

The ALMA-ATOMS survey: vibrationally excited HC_3N lines in hot cores

Li Chen¹, Sheng-Li Qin¹, Tie Liu², Paul F. Goldsmith³, Xunchuan Liu², Yaping Peng⁴, Xindi Tang^{5,6}, Guido Garay^{7,8}, Zhiping Kou^{5,9,1}, Mengyao Tang¹⁰, Patricio Sanhueza^{11,12,13}, Zi-Yang Li^{1,2}, Prasanta Gorai^{14,15}, Swagat R. Das⁷, Leonardo Bronfman⁷, Lokesh Dewangan¹⁶, Pablo García^{17,8}, Shanghuo Li¹⁸, Chang Won Lee^{19,20}, Hong-Li Liu¹, L. Viktor Tóth^{21,22}, James O. Chibueze^{23,24,25}, Jihye Hwang¹⁹, Xiaohu Li^{5,6}, Fengwei Xu^{26,27}, Jiahang Zou^{1,2}, Wenyu Jiao², Zhenying Zhang^{1,2}, and Yong Zhang²⁸

(Affiliations can be found after the references)

ABSTRACT

Context. Interstellar molecules are excellent tools for studying the physical and chemical environments of massive star-forming regions. In particular, vibrationally excited HC_3N (HC_3N^*) lines are the key tracers for probing hot cores environments.

Aims. We present the Atacama Large Millimeter/submillimeter Array (ALMA) 3 mm observations of HC_3N^* lines in 60 hot cores, aiming to investigate how physical conditions affect the excitation of HC_3N^* transitions.

Methods. We have used the XCLASS for line identification. Under the assumption of local thermodynamic equilibrium (LTE), we derived the rotation temperature and column density of HC_3N^* transitions in hot cores. Additionally, we calculated the H_2 column density and number density, along with the abundance of HC_3N^* relative to H_2 , to enable a comparison of the physical properties of hot cores with different numbers of HC_3N^* states.

Results. We have detected HC_3N^* lines in 52 hot cores, in which 29 cores showing more than one vibrationally excited state. Hot cores with higher gas temperatures have more detections of these vibrationally excited lines. The excitation of HC_3N^* requires dense environments, with its spatial distribution influenced by the presence of UC HII regions. The observed column density of HC_3N^* contributes to the number of HC_3N^* states in hot core environments.

Conclusions. After analyzing the various factors influencing HC_3N^* excitation in hot cores, we conclude that the excitation of HC_3N^* is mainly driven by mid-IR pumping, while collisional excitation is ineffective.

Key words. stars: formation – ISM: abundances – ISM: molecules – radio lines: ISM

1. Introduction

Massive star-forming regions represent some of the most dynamic and intriguing environments in the cosmos. These areas serve as cosmic crucibles where gravitational forces, radiation, and turbulent motion interact to shape the birth and evolution of stellar progenitors (Zhang & Li 2017; Tang et al. 2018; Motte et al. 2018; Lu et al. 2020; Yue et al. 2021; Saha et al. 2022; Rosen 2022; Luo et al. 2024)). Motivated by the fundamental importance of massive star-forming regions, researchers have long sought to dissect the molecular landscapes that characterize these environments (for comprehensive reviews, see Herbst & van Dishoeck (2009); Gerin et al. (2016); van Dishoeck (2018); Jørgensen et al. (2020)). Among the myriad molecular species, cyanoacetylene (HC_3N) stands out as a particularly intriguing tracer of dense and warm gas surrounding newly forming stars (Chung et al. 1991; Bergin et al. 1996; Yu et al. 2019) and energetic processes in highly obscured regions (Rico-Villas et al. 2021). Previous observations have laid important groundwork in the investigation of HC_3N lines in massive star-forming regions (Li et al. 2017; Taniguchi et al. 2018; He et al. 2021), shedding light on their abundance patterns, spatial distributions, and excitation mechanisms.

HC_3N ($\text{H}-\text{C}\equiv\text{C}-\text{C}\equiv\text{N}$), the shortest cyanopolyyne, possesses one CN triple bond and one CC triple bond. As a linear molecule, HC_3N is widespread in the interstellar medium (ISM) and has been detected in various astronomical sources both in the Milky

Way (Turner 1971; Kunde et al. 1981; Li & Goldsmith 2012; Velilla Prieto et al. 2015; Zinchenko et al. 2021; Liu et al. 2024) and in external galaxies (Mauersberger et al. 1990; Wang et al. 2020; Martín et al. 2021). The excitation of HC_3N can be driven by the absorption of mid-IR photons and/or collisions with H_2 (Rico-Villas et al. 2020). Because the linear structure of HC_3N lacks a center of symmetry, the spectra produced by its transitions are complex. HC_3N exhibits seven normal vibrations: four stretching vibrations (v_1-v_4) of Σ symmetry and three doubly degenerate bending vibrations (v_5-v_7) of Π symmetry (Mallinson & Fayt 1976). The characteristics of these seven vibrational states are summarized in Table 1 (Ranković et al. 2018). The vibrationally excited state of HC_3N refers to a specific state with higher vibrational energy, resulting from the excitation of a vibrational mode after the molecule absorbs energy. Experiments show that higher vibrational energy levels require a higher impact energy to be collisionally excited (Leach et al. 2014). In astrophysical environments, the critical densities (n_{crit}) for collisional excitation of the $v_7=1$, $v_6=1$, $v_5=1$, and $v_4=1$ levels at 300 K are 4×10^8 , 3×10^{11} , 7×10^{12} , and $2\times 10^{10} \text{ cm}^{-3}$, respectively (Wyrowski et al. 1999). Therefore, in this work, only the low-lying vibrational modes (v_4 , v_5 , v_6 , and v_7) with one or multiple vibrationally excited states have been investigated, as detected in the ALMA band 3 survey.

Despite significant progress, gaps persist in our understanding, particularly in relation to the precise role of vibrationally excited HC_3N (abbreviated as HC_3N^*) in probing the conditions

Table 1: Lowest vibrational modes of HC_3N

Mode	Vibration	Energy ^a	
		(meV)	(K)
v_1	C–H stretch	412	4781
v_2	C≡N stretch	282	3272
v_3	C≡C stretch	257	2982
v_4	C–C stretch	109	1265
v_5	CCH bend	82	952
v_6	CCN bend	62	719
v_7	CCC bend	28	325

^a. The spectroscopic experimental vibrational energies are from Leach et al. (2014)

prevailing within hot cores. Clarifying these issues is essential for constructing comprehensive models of massive star formation and refining our understanding of the underlying physics. Spurred by the potential to unveil crucial details about the physical conditions operating in extreme environments, attention has turned to the study of HC_3N^* lines within hot cores (Goldsmith et al. 1982; Wyrowski et al. 1999; de Vicente et al. 2000; Costagliola & Aalto 2010; Belloche et al. 2013; Peng et al. 2017; Pagani et al. 2017; Taniguchi et al. 2022). The spectral information of the vibrationally excited states can reveal the behavior of HC_3N molecules in different energy states and their distribution in the ISM. Particularly in high-temperature environments, the study of vibrationally excited states is significant for understanding molecular excitation and chemical reaction processes (Esplugues et al. 2013).

Against this backdrop, the primary objective of this paper is to present a detailed examination of HC_3N^* lines in massive star-forming regions and provide a comprehensive understanding of the role HC_3N^* plays in studying the inner physical conditions of hot cores. By systematically exploring the characteristics of different HC_3N^* states, this study intends to elucidate their observational properties and the physical processes shaping their spectral lines. The structure of this paper is organized as follows: In Section 2, we describe the ALMA observations and the data reduction process. Section 3 presents the fundamental results on the detection of HC_3N^* lines and the preliminary analysis of the derived physical parameters. In Section 4, we discuss the results of the study in depth, identifying the physical properties and the vibrational excitation conditions of HC_3N . Finally, Section 5 outlines the key conclusions of this paper.

2. Observations and Data Reduction

2.1. ALMA Observations

The ATOMS, standing for ALMA Three-millimeter Observations of Massive Star-forming regions, is an ALMA Band 3 survey aimed at studying the physical and chemical conditions of 146 massive star-forming regions (Liu et al. 2020) (Project ID: 2019.1.00685.S; PI: Tie Liu). The observations were conducted from September to mid-November 2019 and included both the Atacama Compact 7 m Array (ACA) and the 12 m array (C43-2 or C43-3 configuration). SPWs 7 and 8 are tuned in the upper sideband of the observations, which have a bandwidth of 1875 MHz and a spectral resolution of approximately 1.6 km s⁻¹. SPWs 7 and 8 were primarily used for continuum imaging and line surveys, with center frequencies of $\sim 98,505$ MHz and 100,454 MHz, respectively. In the ATOMS project, due to

the high resolution and minimal flux loss in the dense molecular line tracers, we rely exclusively on 12 m array data to identify molecular lines and hot cores.

2.2. Data Calibration and Imaging

Data reduction and image processing were conducted using version 5.6 of the Common Astronomy Software Applications (CASA) (McMullin et al. 2007). The ACA data and 12 m array data were calibrated separately, and the 12 m array data was chosen for identifying both cloud cores and molecular lines. For the continuum maps, line-free channels were selected in SPW 7 and SPW 8, with a central frequency of approximately 99,404 MHz. Line cubes were produced for each SPW with their native spectral resolution, and the maximum recoverable angular scales were approximately 60 arcsec. All images were corrected for primary beam. The 12 m data for the 146 clumps have an angular resolution of approximately 1.2–1.9 arcsec (the linear scale angular resolution are listed in column 4 of Table 3 to Table 6), with a mean sensitivity of approximately 0.4 mJy beam⁻¹ for continuum and better than 10 mJy beam⁻¹ per channel for lines. By utilizing three complex organic molecules (COMs), namely $\text{C}_2\text{H}_5\text{CN}$, CH_3OCHO , and CH_3OH , as probes for hot cores, Qin et al. (2022) successfully identified 60 hot cores, which have been selected as the sample for our study.

3. Methods and Results

3.1. HC_3N^* line identification

We conducted a search for all vibrationally excited lines of HC_3N in 60 hot cores. The molecular lines were obtained from the peak position of each hot core. Precise line identification was performed using the eXtended CASA Line Analysis Software Suite (XCLASS, (Möller et al. 2017))¹, assuming local thermodynamic equilibrium (LTE). The Cologne Database for Molecular Spectroscopy (CDMS, (Müller et al. 2001, 2005; Endres et al. 2016))², and the Jet Propulsion Laboratory (JPL) molecular databases (Pickett et al. 1998)³, accessed through XCLASS, provided line parameters such as rest frequency, quantum number (QN), dipole-weighted transition dipole matrix elements ($S_{ij}\mu^2$), Einstein A coefficient (A_{ij}), and upper energy (E_u). In this survey, we have detected a total of 7 types of HC_3N^* lines in 52 hot cores: $v_7=1$, $v_7=2$, $v_7=3$, $v_6=1$, $v_6=v_7=1$, $v_5=1$, and $v_4=1$. The 7 HC_3N states include 18 transitions in SPW 8 and none in SPW 7, all corresponding to the same $J=11–10$ transition. The relevant parameters are listed in Table A.1. One HC_3N $v=0$ ($J=11–10$) line was also detected in SPW 8 at the rest frequency $\sim 100,076$ MHz, pointing to all 52 hot cores containing HC_3N molecules. The determination of each line was based on its velocity offset, which was almost the same as the source's systemic velocity (see Liu et al. (2020) for specific values), and with a line intensity above the 3σ detection level.

The distribution of HC_3N^* lines is concentrated in SPW 8, with broad range of upper energy levels ranging from 349 to 1274 K. We used XCLASS to fit the physical parameters, including rotation temperature, column density, line width, and velocity offset, by setting the deconvolved size of the continuum core, rotation temperature, source-averaged column density, line width, and velocity offset as free parameters into the fitting pro-

¹ <https://xclass.astro.uni-koeln.de/>

² <https://cdms.astro.uni-koeln.de/>

³ <http://spec.jpl.nasa.gov>

Table 2: Physical parameters derived from vibrationally excited HC_3N lines

Source	$v_7=1$	$v_7=2$	$v_6=1$	$v_5=1$	$v_7=3$	$v_6=v_7=1$	$v_4=1$	Excitation	T_{rot} (K)	$N (\text{cm}^{-2})$
I08303-4303	×	×	×	×	×	×	×	0
I08470-4243	✓	×	×	×	×	×	×	1
I09018-4816	×	×	×	×	×	×	×	0
I11298-6155	×	×	×	×	×	×	×	0
I12326-6245	✓	✓	×	×	×	×	×	2	189 ± 16	$(1.3 \pm 0.1) \times 10^{16}$
I13079-6218	✓	✓	✓	✓	✓	✓	✓	6	253 ± 14	$(2.8 \pm 0.1) \times 10^{16}$
I13134-6242	✓	✓	✓	✓	✓	✓	✓	6	335 ± 22	$(1.9 \pm 0.1) \times 10^{16}$
I13140-6226	✓	×	×	×	×	×	×	1
I13471-6120	✓	×	×	×	×	×	×	1
I13484-6100	✓	×	×	×	×	×	×	1
I14498-5856	✓	×	×	×	×	×	×	1
I15254-5621	✓	×	×	×	×	×	×	1
I15437-5343	✓	×	×	×	×	×	×	1
I15520-5234	✓	×	×	×	×	×	×	1
I16060-5146	✓	✓	✓	✓	✓	✓	✓	3	307 ± 33	$(9.1 \pm 0.1) \times 10^{15}$
I16065-5158	✓	✓	✓	✓	✓	✓	✓	6	248 ± 21	$(4.7 \pm 0.1) \times 10^{16}$
I16071-5142	✓	✓	✓	✓	✗	✗	✗	3	161 ± 18	$(1.4 \pm 0.1) \times 10^{16}$
I16076-5134	✓	✓	✓	✓	✗	✗	✗	3	160 ± 12	$(7.8 \pm 0.1) \times 10^{15}$
I16164-5046	✓	✓	✓	✓	✗	✗	✗	3	262 ± 34	$(8.8 \pm 0.1) \times 10^{15}$
I16172-5028	✓	×	×	×	✗	✗	✗	1
I16272-4837c1	✓	✓	✓	✓	✗	✗	✗	3	169 ± 32	$(1.9 \pm 0.1) \times 10^{16}$
I16272-4837c2	✓	×	×	×	✗	✗	✗	1
I16272-4837c3	✓	×	×	×	✗	✗	✗	1
I16318-4724	✓	✓	✓	✓	✓	✓	✓	6	229 ± 12	$(2.9 \pm 0.2) \times 10^{16}$
I16344-4658	✓	×	×	×	✗	✗	✗	1
I16348-4654	✓	✓	✓	✓	✓	✓	✓	7	313 ± 12	$(1.5 \pm 0.1) \times 10^{17}$
I16351-4722	✗	×	×	×	✗	✗	✗	0
I16458-4512	✗	×	×	×	✗	✗	✗	0
I16484-4603	✓	×	×	×	✗	✗	✗	1
I16547-4247	✓	✓	✓	✓	✓	✓	✓	6	277 ± 32	$(2.6 \pm 0.1) \times 10^{16}$
I17008-4040	✓	✓	✓	✓	✓	✓	✓	6	224 ± 14	$(2.3 \pm 0.1) \times 10^{16}$
I17016-4124c1	✓	✓	✓	✓	✗	✗	✗	3	190 ± 20	$(2.5 \pm 0.1) \times 10^{16}$
I17016-4124c2	✗	×	×	×	✗	✗	✗	0
I17158-3901c1	✓	×	×	×	✗	✗	✗	1
I17158-3901c2	✓	×	×	×	✗	✗	✗	1
I17175-3544	✓	✓	✓	✓	✓	✓	✓	6	321 ± 8	$(4.2 \pm 0.1) \times 10^{16}$
I17220-3609	✓	✓	✓	✓	✗	✗	✗	3	165 ± 15	$(1.8 \pm 0.1) \times 10^{16}$
I17233-3606	✓	✓	✓	✓	✓	✓	✓	5	185 ± 9	$(2.7 \pm 0.1) \times 10^{16}$
I17441-2822	✓	✓	✓	✓	✓	✓	✓	6	232 ± 28	$(3.8 \pm 0.1) \times 10^{16}$
I18032-2032c1	✗	×	×	✗	✗	✗	✗	0
I18032-2032c2	✓	✓	✓	✓	✓	✓	✓	6	210 ± 7	$(1.4 \pm 0.1) \times 10^{16}$
I18032-2032c3	✓	×	×	✗	✗	✗	✗	1
I18032-2032c4	✓	×	×	✗	✗	✗	✗	1
I18056-1952	✓	✓	✓	✓	✓	✓	✓	7	270 ± 5	$(1.7 \pm 0.1) \times 10^{18}$
I18089-1732	✓	✓	✓	✓	✓	✓	✓	6	276 ± 37	$(3.2 \pm 0.1) \times 10^{16}$
I18117-1753	✓	✓	✓	✓	✗	✗	✗	3	165 ± 8	$(1.8 \pm 0.1) \times 10^{16}$
I18159-1648c1	✓	×	×	✗	✗	✗	✗	1
I18159-1648c2	✓	×	×	✗	✗	✗	✗	1
I18182-1433	✓	×	×	✗	✗	✗	✗	1
I18236-1205	✓	×	×	✗	✗	✗	✗	1
I18290-0924	✗	×	×	✗	✗	✗	✗	0
I18316-0602	✓	✓	✓	✓	✗	✗	✗	3	244 ± 22	$(7.1 \pm 0.1) \times 10^{15}$
I18411-0338	✓	✓	✓	✓	✓	✓	✓	6	273 ± 7	$(2.2 \pm 0.1) \times 10^{16}$
I18469-0132	✓	✓	✓	✗	✗	✗	✗	2	239 ± 67	$(1.1 \pm 0.3) \times 10^{16}$
I18507+0110	✓	✓	✓	✓	✓	✓	✓	6	245 ± 19	$(7.6 \pm 0.1) \times 10^{16}$
I18507+0121	✓	✓	✓	✓	✓	✓	✓	6	218 ± 20	$(2.1 \pm 0.1) \times 10^{16}$
I18517+0437	✓	×	×	✗	✗	✗	✗	1
I19078+0901c1	✓	✓	✓	✗	✗	✗	✗	3	235 ± 48	$(6.9 \pm 0.3) \times 10^{15}$
I19078+0901c2	✓	✓	✓	✗	✗	✗	✗	3	217 ± 14	$(1.1 \pm 0.1) \times 10^{16}$
I19095+0930	✓	×	×	✗	✗	✗	✗	1

Notes: Column 1 lists the source names. From column 2 to column 8, the ✓ marks the existence and the ✗ marks the inexistence of a HC_3N^* state. In column 9, the number of Excitation means the number of excited HC_3N^* states for each hot core. Columns 10 and 11 list the fitted rotation temperature and column density for HC_3N^* states.

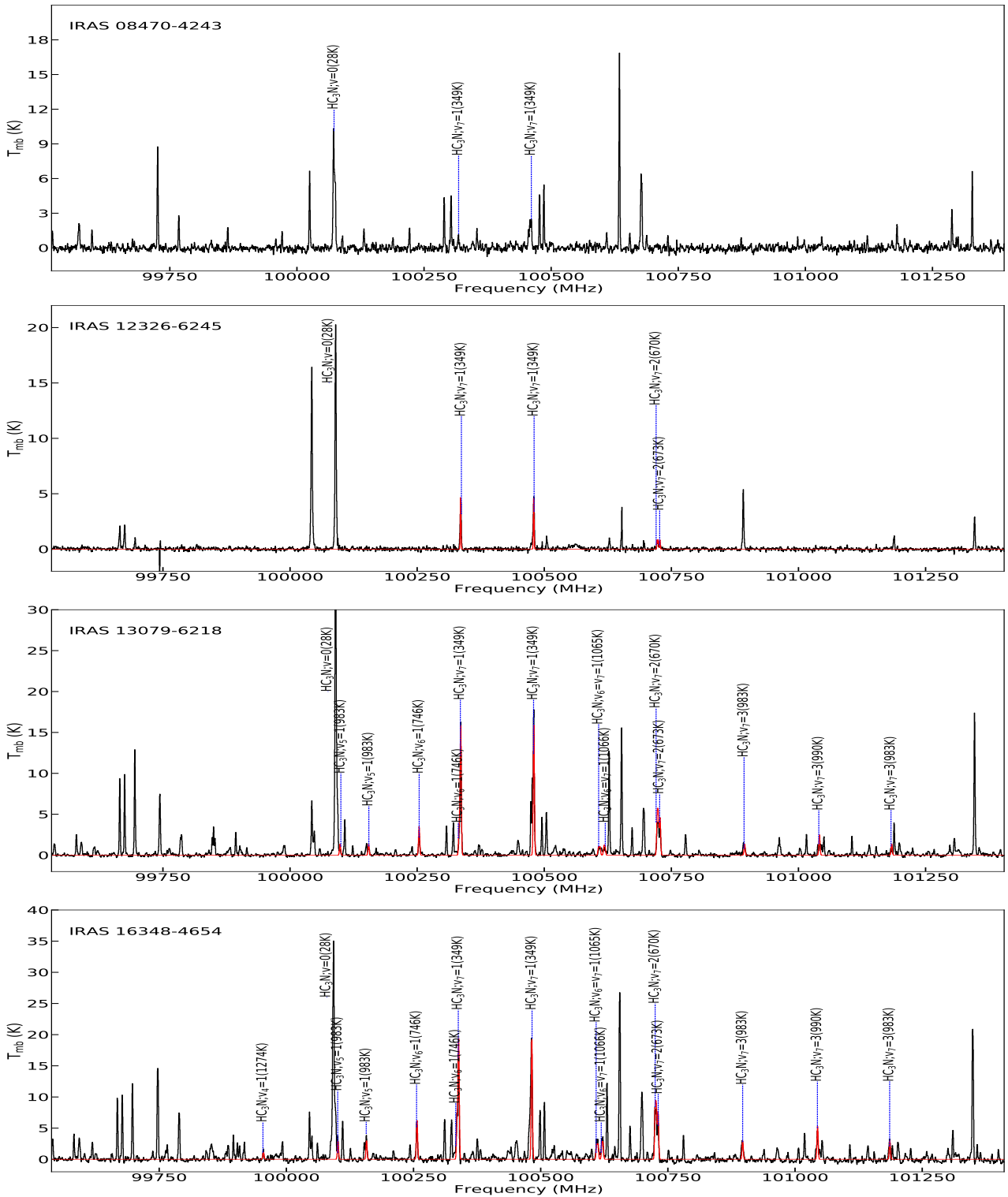


Fig. 1: Sample spectra of HC_3N^* in SPW 8 for four typical hot cores. The black lines show the observed spectra at sky frequencies and the red lines show the XCLASS modeled spectra using the best-fit parameters for vibrationally excited HC_3N lines. The complete spectra in SPW 8 for other hot cores are available in Figure B.1.

cess, with a setup of an isotope ratio of 1 (i.e., the same abundance) for HC_3N^* in each vibrationally excited state. Physical parameters for each vibrationally excited state were determined simultaneously only when there were three or more corresponding lines. However, for hot cores with only $v_7=1$ lines, it was not possible to derive the physical parameters as only 2 emis-

sion lines were detected. Ultimately, we were able to fit 29 hot cores with more than 3 vibrationally excited lines. The catalog of detected HC_3N^* lines towards hot cores, along with the corresponding rotation temperatures and column densities, is presented in Table 2. Among the 60 hot cores in our sample, 8 show no HC_3N^* emission, accounting for 13% of the total detections.

Additionally, 23 display exclusively $v_7 = 1$ emission, representing 38% of the total hot core detections. The detection rates for $v_7=1$, $v_7=2$, $v_6=1$, $v_5=1$, $v_7=3$, $v_6=v_7=1$, and $v_4=1$ are 87%, 48%, 45%, 27%, 27%, 25%, and 3%, respectively. In Figure 1, we present sample spectra of HC_3N towards four representative hot cores, each with varying numbers of HC_3N^* states, along with the modeled spectra based on the best-fitting parameters. The differences in excitation of different vibrationally excited lines may be attributed to variations in the physical environments of the sources.

3.2. Core parameters

3.2.1. Continuum flux

Ultra-compact (UC) HII regions are manifestations of newly formed massive stars that are still embedded in their natal molecular clouds (Churchwell 2002). For hot cores without UC HII regions, the continuum flux is mainly contributed by dust emission. We used 2D Gaussian fitting in CASA to determine the deconvolved core size, where the full width at half maximum (FWHM) along the major and minor axes are denoted as θ_{maj} and θ_{min} , respectively. An effective core radius R_{core} was calculated using $R_{\text{core}} = \sqrt{\theta_{\text{maj}} \times \theta_{\text{min}}}$. Simultaneously, we obtained the integrated flux S_{ν}^{int} and the peak flux S_{ν}^{peak} of the hot core. The parameters R_{core} , S_{ν}^{int} and S_{ν}^{peak} for hot cores without UC HII regions are listed in columns 5, 7, and 8 of Tables 3 and 4.

For hot cores associated with UC HII regions, we need to subtract the flux of free-free emission of the UC HII regions from the observed continuum maps to obtain the corrected flux of dust emission. The UC HII regions were identified using the $\text{H}40\alpha$ line at 99,023 MHz from SPW 7 (Liu et al. 2021; Qin et al. 2022). We assumed the free-free continuum is optically thin at 99,023 MHz. Thus, we can estimate the intensity of free-free continuum emission under LTE assumption via (Condon & Ransom 2016):

$$S_{\text{ff}} = 1.43 \times 10^{-3} \nu^{-1.1} T_e^{1.15} [1 + \frac{N(\text{He}^+)}{N(\text{H}^+)}] \int S_{\text{H}40\alpha} dv, \quad (1)$$

where S_{ff} is the intensity of free-free continuum emission, $\nu = 99.023$ GHz near the center frequency of the continuum map, T_e is the electron temperature which is assumed as 6000K (Shaver 1970; Afflerbach et al. 1996; Khan et al. 2022), $N(\text{He}^+)/N(\text{H}^+) \approx 0.08$ is the typical ratio, and $\int S_{\text{H}40\alpha} dv$ is the integrated intensity of the $\text{H}40\alpha$ line. Since molecular gas emission is invariably associated with the presence of dust, this method might slightly overestimate the free-free contribution to the emission from these sources (Bonfand et al. 2024).

We use the observed continuum emission to subtract the free-free continuum emission and get the true flux from the dust:

$$S_{\text{dust}} = S_{\text{obs}} - S_{\text{ff}}, \quad (2)$$

The parameters R_{core} , S_{ν}^{int} and S_{ν}^{peak} for hot cores associated with UC HII regions are listed in columns 5, 7 and 8 of Tables 5 and 6. After the correction of dust flux, it is found that I18032–2032 core1 and core 4 show almost no dust emission, indicating that the continuum flux is mainly dominated by free-free emission.

3.2.2. Parameter calculation

The mass of each core can be calculated as follows (Hildebrand 1983):

$$M_{\text{core}} = \frac{D^2 S_{\nu}^{\text{int}} \eta}{\kappa_{\nu} B_{\nu}(T_d)}, \quad (3)$$

where D is the distance to the source, S_{ν}^{int} represents the integrated flux of the dust core, η is the gas-to-dust ratio increases with galactocentric distance R_{GC} , which have been described by (Giannetti et al. 2017; Taniguchi et al. 2023):

$$\log(\eta) = (0.087 \pm 0.007) R_{\text{GC}} + (1.44 \pm 0.03), \quad (4)$$

where the R_{GC} of cores can be referred from Liu et al. (2020), the dust absorption coefficient κ_{ν} for molecular cloud cores is interpolated to be $0.24 \text{ cm}^2 \text{ g}^{-1}$ at 99,000 MHz (Ossenkopf & Henning 1994), and $B_{\nu}(T_d)$ is the Planck function at the dust temperature T_d (see footnote a of Table 3 for selection criteria of T_d).

From the 3 mm continuum maps, the source-averaged column density of H_2 (N_{H_2}) can be derived as below (Frau et al. 2010; Bonfand et al. 2019):

$$N_{\text{H}_2} = \frac{S_{\nu}^{\text{int}} \eta}{\mu m_{\text{H}} \Omega \kappa_{\nu} B_{\nu}(T_d)}, \quad (5)$$

where $\mu \approx 2.8$ is the mean particle weight per H_2 molecule (Kauffmann et al. 2008), m_{H} is the mass of a hydrogen atom and Ω is the solid angle covered by the source.

Meanwhile, after the determination of M_{core} , the number density of H_2 , $n(\text{H}_2)$, can be derived by:

$$n(\text{H}_2) = \frac{M_{\text{core}}}{(4/3)\pi \mu m_{\text{H}} R_{\text{core}}^3}, \quad (6)$$

Table 3 to table 6 list the core mass, H_2 column density, H_2 number density and abundance of HC_3N^* with respect to H_2 . The source-averaged column density of HC_3N^* ranges from $(6.9 \pm 0.3) \times 10^{15}$ to $(1.7 \pm 0.1) \times 10^{18} \text{ cm}^{-2}$. It is noteworthy that the HC_3N^* column density of I18056-1952 is at least one order of magnitude higher than other hot cores, while the average column density of the remaining hot cores is $(2.7 \pm 0.1) \times 10^{16} \text{ cm}^{-2}$. There are no significant differences in column density between hot cores associated with and without UC HII regions. The calculated N_{H_2} of the 52 hot cores containing HC_3N^* ranges from $(5.3 \pm 0.2) \times 10^{22}$ to $(2.0 \pm 0.2) \times 10^{25} \text{ cm}^{-2}$, while that of the 8 hot cores not containing HC_3N^* ranges from $(8.5 \pm 0.5) \times 10^{22}$ to $(3.8 \pm 0.5) \times 10^{24} \text{ cm}^{-2}$. Then for the fitted 29 hot cores, the abundance $f_{\text{HC}_3\text{N}^*}$ ranges from $(6.9 \pm 1.5) \times 10^{-10}$ to $(2.3 \pm 0.2) \times 10^{-7}$. The $n(\text{H}_2)$ of hot cores containing HC_3N^* ranges from $(1.3 \pm 0.2) \times 10^5$ to $(5.0 \pm 0.5) \times 10^8 \text{ cm}^{-3}$, with a mean value of $3.2 \times 10^7 \text{ cm}^{-3}$. The high $n(\text{H}_2)$ indicates that the excitation of HC_3N^* occurs in the dense core regions of molecular clouds.

In addition to using XCLASS for parameter fitting, we also conducted a rotational temperature diagram (RTD) analysis to determine the rotation temperature of the observed HC_3N^* lines (Goldsmith & Langer 1999). Figure C.1 shows the RTD for HC_3N^* lines across 29 hot cores, all of which were also analyzed with XCLASS. Considering the errors, the rotation temperatures obtained via RTD are consistent with those derived from XCLASS, supporting the reliability of our fitted rotation temperatures.

Table 3: The basic physical parameters of hot cores without UC HII regions which show HC₃N* emission.

Source	Distance (kpc)	R _{GC} (kpc)	Resolution (au)	R _{core} (au)	T _d ^a (K)	S _v ^{int} (mJy)	S _v ^{peak} (mJy beam ⁻¹)	M _{core} (M _⊙)	N _{H₂} (cm ⁻³)	n(H ₂) (cm ⁻³)	f _{HC₃N*}
I08470-4243	2.10	8.8	2520	3780	200±30	37.8±2.3	18.8±0.7	9.0±1	(3.8±0.6)×10 ²³	(5.0±0.8)×10 ⁶	...
I13079-6218	3.80	6.9	4560	9120	110±9	109.5±2.9	62.5±0.9	106.8±9	(7.8±0.7)×10 ²³	(4.3±0.4)×10 ⁶	(3.6±0.3)×10 ⁻⁸
I13134-6242	3.80	6.9	6460	8360	160±5	143.1±2.3	86.1±0.9	95.3±4	(8.2±0.3)×10 ²³	(4.9±0.2)×10 ⁶	(2.3±0.2)×10 ⁻⁸
I13140-6226	3.80	6.9	6460	20900	120±17	44±2.4	12.7±0.6	39.3±6	(5.4±0.8)×10 ²²	(1.3±0.2)×10 ⁵	...
I13484-6100	5.40	6.4	9720	13500	131±18	51.2±1.7	23.7±0.6	76.3±11	(2.5±0.4)×10 ²³	(9.4±1.3)×10 ⁵	...
I14498-5856	3.16	6.4	5688	8848	106±3	67.3±3.1	27.4±0.9	42.6±2	(3.3±0.2)×10 ²³	(1.9±0.1)×10 ⁶	...
I15437-5343	4.98	5.0	8466	11454	106±11	29.6±0.5	15.1±0.2	35.2±4	(1.6±0.2)×10 ²³	(7.1±0.8)×10 ⁵	...
I16272-4837c1	2.92	5.8	4964	6424	230±37	127±6.4	63.9±2.2	27.7±5	(4.1±0.7)×10 ²³	(3.2±0.5)×10 ⁶	(4.7±0.8)×10 ⁻⁸
I16272-4837c2	2.92	5.8	4964	5840	150±9	19.3±0.9	9.5±0.3	6.5±1	(1.2±0.1)×10 ²³	(9.9±0.8)×10 ⁵	...
I16272-4837c3	2.92	5.8	4964	6132	123±12	19.1±0.7	9.5±0.3	7.9±1	(1.3±0.1)×10 ²³	(1.0±0.1)×10 ⁶	...
I16318-4724	7.68	3.3	13056	16896	148±15	104±3.2	49.4±1.1	148.9±16	(3.2±0.3)×10 ²³	(9.4±1.0)×10 ⁵	(9.2±1.2)×10 ⁻⁸
I16344-4658	12.09	5.4	20553	20553	160±15	54.2±1.4	31.5±0.7	270.5±27	(3.9±0.4)×10 ²³	(9.4±0.9)×10 ⁵	...
I16484-4603	2.10	6.4	3570	2730	127±5	65.0±1.0	45.0±0.4	15.1±1	(1.2±0.1)×10 ²⁴	(2.3±0.1)×10 ⁷	...
I16547-4247	2.74	5.8	5206	6850	150±20	160.8±6.1	74.8±2.1	47.7±7	(6.1±0.9)×10 ²³	(4.5±0.6)×10 ⁶	(4.2±0.6)×10 ⁻⁸
I17008-4040	2.38	6.1	4522	4046	150±14	94.2±3.4	58.7±1.2	22.4±2	(8.3±0.8)×10 ²³	(1.0±0.1)×10 ⁷	(2.8±0.3)×10 ⁻⁸
I17158-3901c1	3.38	5.1	5746	9802	151±12	64.6±2.3	54.6±0.7	25.2±2	(1.6±0.1)×10 ²³	(8.1±0.7)×10 ⁵	...
I17158-3901c2	3.38	5.1	5746	9464	152±3	20.3±0.7	10.2±0.2	7.9±1	(5.3±0.2)×10 ²²	(2.8±0.1)×10 ⁵	(4.2±0.6)×10 ⁻⁸
I17233-3606	1.34	7.0	2278	5226	100±14	596±22	130.9±3.7	81.3±12	(1.8±0.3)×10 ²⁴	(1.7±0.3)×10 ⁷	(1.5±0.2)×10 ⁻⁸
I18032-2032c2	5.15	3.4	7725	12360	130±12	57.1±5.9	17.8±1.4	42.8±6	(1.7±0.2)×10 ²³	(6.9±0.1)×10 ⁵	(8.3±1.3)×10 ⁻⁸
I18032-2032c3	5.15	3.4	7725	5665	110±3	34.7±3	7.4±0.6	30.8±3	(5.8±0.5)×10 ²³	(5.1±0.5)×10 ⁶	...
I18056-1952	8.55	1.6	12825	9405	133±5	767±8.4	600.3±4.3	1079.2±53	(7.4±0.4)×10 ²⁴	(3.9±0.2)×10 ⁷	(2.3±0.2)×10 ⁻⁷
I18089-1732	2.50	5.9	4250	4250	128±14	80.1±2.7	45.8±1.1	23.7±3	(7.9±0.9)×10 ²³	(9.4±1.1)×10 ⁶	(4.0±0.5)×10 ⁻⁸
I18117-1753	2.57	5.9	4369	4112	160±25	38.4±1.6	22.5±0.5	9.6±2	(3.4±0.6)×10 ²³	(4.2±0.7)×10 ⁶	(5.3±0.9)×10 ⁻⁸
I18159-1648c1	1.48	6.9	2516	2516	161±18	84.9±6.9	36.5±1.4	8.5±1	(8.1±1.1)×10 ²³	(1.6±0.2)×10 ⁷	...
I18159-1648c2	1.48	6.9	2516	2812	110±22	73.8±5.3	21.2±1.2	10.9±2	(8.4±1.8)×10 ²³	(1.5±0.3)×10 ⁷	...
I18182-1433	4.71	4.1	8007	9891	122±4	62.5±1.6	29.2±0.5	48.1±2	(3.0±0.1)×10 ²³	(1.5±0.1)×10 ⁶	...
I18236-1205	2.17	6.3	3689	3038	110±8	18±0.48	11.6±0.2	5.1±1	(3.3±0.3)×10 ²³	(5.5±0.4)×10 ⁶	...
I18316-0602	2.09	6.5	3135	6061	108±204	57.7±3.2	24.8±1	16.0±3	(2.6±0.5)×10 ²³	(2.2±0.4)×10 ⁶	(2.7±0.5)×10 ⁻⁸
I18411-0338	7.41	4.0	11115	7410	160±15	24.6±1.1	17.7±0.5	34.8±4	(3.8±0.4)×10 ²³	(2.6±0.3)×10 ⁶	(5.7±0.7)×10 ⁻⁸
I18507+0121	1.56	7.1	2340	2652	200±12	103.3±3	61.3±1.2	9.6±1	(8.3±0.6)×10 ²³	(1.6±0.1)×10 ⁷	(2.5±0.2)×10 ⁻⁸
I18517+0437	2.36	6.6	3540	5428	140±23	32.3±1.8	15.0±0.7	8.9±2	(1.8±0.3)×10 ²³	(1.7±0.3)×10 ⁶	...
I19078+0901c2	11.11	7.6	16665	19998	115±6	90±21	53.8±8.2	824.9±197	(1.2±0.3)×10 ²⁴	(3.1±0.9)×10 ⁶	(8.8±2.3)×10 ⁻⁹

^a The dust temperature is adopted from the temperature of COMs (CH₃OCHO, C₂H₅CN, and CH₃OH) calculated by Qin et al. (2022). The temperature selection for each source is: prioritize CH₃OCHO if available, otherwise select C₂H₅CN, and choose CH₃OH if it is the only one present. The same selection criteria apply to Table 4, Table 5, and Table 6.

Table 4: The basic physical parameters of hot cores without UC Hn regions without HC_3N^* emission.

Source	Distance (kpc)	R_{GC} (kpc)	Resolution (au)	R_{core} (au)	T_{d} (K)	S_{ν}^{int} (mJy)	S_{ν}^{peak} (mJy beam $^{-1}$)	M_{core} (M_{\odot})	N_{H_2} (cm $^{-2}$)	$n(\text{H}_2)$ (cm $^{-3}$)
I08303-4303	2.30	9.0	2760	5060	101±9	29.1±4.3	8.7±0.3	17.3±3	(4.1±0.7)×10 23	(4.0±0.7)×10 6
I09018-4816	2.60	8.8	3120	8840	160±8	161±22	13.0±0.6	73.4±11	(5.7±0.8)×10 23	(3.2±0.5)×10 6
I11298-6155	10.00	10.1	18000	31000	124±6	42.6±2.5	19.0±0.8	483.4±37	(3.0±0.2)×10 23	(4.9±0.4)×10 5
I16458-4512	3.56	5.1	6052	3916	120±4	178.6±2.8	136.1±1.3	97.5±4	(3.8±0.2)×10 24	(4.9±0.2)×10 7
I18290-0924	5.34	4.0	8010	7476	120±4	8.0±0.3	6.1±0.2	7.9±1	(8.5±0.5)×10 22	(5.7±0.3)×10 5

Table 5: The basic physical parameters of hot cores associated with UC Hn regions which show HC_3N^* emission

Source	Distance (kpc)	R_{GC} (kpc)	Resolution (au)	R_{core} (au)	T_{d} (K)	S_{ν}^{int} (mJy)	S_{ν}^{peak} (mJy beam $^{-1}$)	M_{core} (M_{\odot})	N_{H_2} (cm $^{-2}$)	$n(\text{H}_2)$ (cm $^{-3}$)	$f_{\text{HC}_3\text{N}^*}$
I12326-6245	4.61	7.2	7837	8298	137±33	620±53	337±20	755.6±193	(6.6±1.7)×10 24	(4.0±1.0)×10 7	(2.0±0.5)×10 $^{-9}$
I13471-6120	5.46	6.4	9828	5460	126±10	121.2±9.6	106.2±5	192.2±22	(3.9±0.4)×10 24	(3.6±0.4)×10 7	...
I15254-5621	4.00	5.7	7200	3200	146±14	247±12	201.6±6.3	157.3±17	(9.3±1.0)×10 24	(1.5±0.2)×10 8	...
I15520-5234	2.65	6.2	4505	7685	160±30	153±20	106.9±9.1	43.1±10	(4.4±1.0)×10 23	(2.9±0.7)×10 6	...
I16060-5146	5.30	4.5	9010	10070	110±22	110.6±91	685±37	1297.4±281	(7.7±1.7)×10 24	(3.9±0.8)×10 7	(1.2±0.3)×10 $^{-9}$
I16065-5158	3.98	5.2	6766	12338	150±43	225±17	85.8±4.9	124.9±37	(5.0±1.5)×10 23	(2.0±0.6)×10 6	(9.5±2.8)×10 $^{-8}$
I16071-5142	5.30	4.5	9010	22260	150±20	174±11	64.3±3.1	148.8±22	(1.8±0.3)×10 23	(4.1±0.6)×10 5	(7.7±1.3)×10 $^{-8}$
I16076-5134	5.30	4.5	9010	22790	121±32	87±11	21.9±2.2	92.6±27	(1.1±0.3)×10 23	(2.4±0.7)×10 5	(7.2±2.1)×10 $^{-8}$
I16164-5046	3.57	5.4	6069	9996	157±19	702±58	214±14	311.5±46	(1.9±0.3)×10 24	(9.5±1.4)×10 6	(4.7±0.7)×10 $^{-9}$
I16172-5028	3.57	5.4	6069	6426	110±32	643±38	475±18	409.8±122	(6.0±1.8)×10 24	(4.7±1.4)×10 7	...
I16348-4654	12.09	5.4	20553	9672	213±12	167.2±5.6	135.3±2.8	624.6±42	(4.0±0.3)×10 24	(2.1±0.1)×10 7	(3.7±0.4)×10 $^{-8}$
I17016-4124c1	1.37	7.0	2603	1233	143±14	155±23	85.4±8.6	15.3±3	(6.1±1.1)×10 24	(2.5±0.4)×10 8	(4.1±0.8)×10 $^{-9}$
I17175-3544	1.34	7.0	2278	4556	183±8	622±68	247±20	45.9±5	(1.3±0.2)×10 24	(1.5±0.2)×10 7	(3.1±0.4)×10 $^{-8}$
I17220-3609	8.01	1.3	13617	12816	173±22	255±40	75.2±9.3	227.0±46	(8.4±1.7)×10 23	(3.3±0.7)×10 6	(2.2±0.5)×10 $^{-8}$
I17441-2822	8.10	0.2	11340	10530	144±7	2150±100	1240±41	1891.8±146	(1.0±0.1)×10 25	(4.9±0.4)×10 7	(3.7±0.3)×10 $^{-9}$
I18032-2032c4	5.15	3.4	7725	10815	140±13
I18469-0132	5.16	4.7	7740	4644	136±15	68.1±8.3	32.7±2.8	63.5±10	(1.8±0.3)×10 24	(1.9±0.3)×10 7	(6.2±2.0)×10 $^{-9}$
I18507+0110	1.56	7.1	2340	2028	200±11	1490±120	682±40	138.8±14	(2.0±0.2)×10 25	(5.0±0.5)×10 8	(3.7±0.4)×10 $^{-9}$
I19078+0901c1	11.11	7.6	16665	18887	140±22	784±109	376±37	5881.0±1235	(1.0±0.2)×10 25	(2.6±0.6)×10 7	(6.9±1.5)×10 $^{-10}$
I19095+0930	6.02	5.8	9030	3010	121±3	101.5±5.9	95.5±3.2	180.8±12	(1.2±0.1)×10 25	(2.0±0.1)×10 8	...

Table 6: The basic physical parameters of hot cores associated with UC Hn regions without HC_3N^* emission.

Source	Distance (kpc)	R_{GC} (kpc)	Resolution (au)	R_{core} (au)	T_{d} (K)	S_{ν}^{int} (mJy)	S_{ν}^{peak} (mJy beam $^{-1}$)	M_{core} (M_{\odot})	N_{H_2} (cm $^{-2}$)	$n(\text{H}_2)$ (cm $^{-3}$)
I16351-4722	3.02	5.7	5134	4530	150±31	174±15	31±2.4	61.4±14	(1.8±0.4)×10 24	(2.0±0.4)×10 7
I17016-4124c2	1.37	7.0	2603	2466	165±32	134.3±3.8	79.7±1.5	11.5±2	(1.1±0.2)×10 24	(2.3±0.5)×10 7
I18032-2032c1	5.15	3.4	7725	4635	204±17

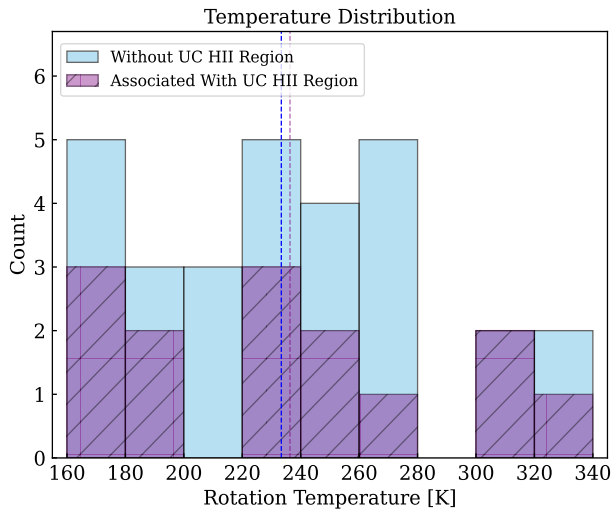


Fig. 2: Histogram of rotation temperatures of vibrationally excited HC_3N lines observed in hot cores. The purple and skyblue bars present the number of cores associated with and without UC $\text{H}\alpha$ regions. The dashed blue line indicates the average rotation temperature of 233 K for hot cores without UC $\text{H}\alpha$ regions and the dashed purple line indicates the average rotation temperature of 236 K for hot cores associated with UC $\text{H}\alpha$ regions.

Figure 2 illustrates the rotation temperature distribution of 29 fitted hot cores derived from the XCLASS fit. From our samples, the rotation temperature ranges from (160 ± 18) to (335 ± 22) K, with a mean value of (235 ± 21) K. The median temperature of (235 ± 48) K is the same as the mean value, indicating that the rotation temperature distribution may be close to symmetric. Furthermore, the mean rotation temperatures of HC_3N^* molecule in hot cores associated with and without UC $\text{H}\alpha$ regions are (236 ± 17) K and (233 ± 25) K, respectively, showing no significant difference. This suggests that the presence of UC $\text{H}\alpha$ regions likely does not affect the rotation temperature of HC_3N^* molecule.

3.3. Spatial distributions

Figure 3 shows the example moment zero maps of 7 HC_3N^* states of hot cores in IRAS 16348–4654 and IRAS 18056–1952, two sources that detected the seven types of emission, for the analysis of spatial distributions of HC_3N^* molecules in hot cores. Because these lines selected to create moment 0 maps are not contaminated by other molecular emissions, the resulting distribution is entirely of the vibrationally excited states. The moment zero maps somewhat suggest that we can recognize a general similarity in the spatial distribution of various types of HC_3N^* emission. Emissions from different energy levels all originate from the central region of the molecular core, with almost no differences in their spatial distribution. However, since these two sources are located at very large distances, we were unable to resolve the emission distribution with 3 mm data. Besides, it is clearly observed that higher upper energy levels exhibit lower integrated intensities of vibrational excitation, indicating an inverse relationship between the observed excitation intensity and the upper energy level. This also implies that it becomes increasingly difficult to excite higher energy levels.

Higher angular resolution data will reveal the actual distribution of these transitions, allowing us to infer the physical and chemical properties in much greater detail, which is beyond the scope of this work.

Using the $\text{H}40\alpha$ line at 99,023 MHz from SPW 7, we identified 20 hot cores affected by ionized hydrogen gas emission. As shown in Figure 4, the HC_3N^* molecular emission peaks and the continuum cores consistently shift in regions associated with UC $\text{H}\alpha$ regions. Among the 20 hot cores with UC $\text{H}\alpha$ regions, 6 cases (I12326-6245, I16060-5146, I16076-5134, I16348-4654, I17175-3544, and I17441-2822) displayed significant separations greater than 4500 au, 11 cases (I13471-6120, I15254-5621, I15520-5234, I16065-5158, I16071-5142, I16164-5046, I16172-5028, I17016-4124, I17220-3609, I18507+0110, and I19078+0901c1) showed relatively small separations less than 4500 au, and 3 cases (I18032-2032c4, I18469-0132, and I19095+0930) were aligned with the $\text{H}40\alpha$ peak. Figure 5 illustrates the spatial distribution of HC_3N^* molecules in hot cores without UC $\text{H}\alpha$ region. It is clear that among the hot cores without UC $\text{H}\alpha$ regions, 28 sources exhibited consistent alignment, while only 4 sources (I13484-6100, I16344-4658, I17233-3606, and I18182-1433) showed minor peak shifts, with separations of less than 4500 au.

4. Discussion

4.1. The role of UC $\text{H}\alpha$ regions

The intense ultraviolet (UV) radiation and associated pressure originating from UC $\text{H}\alpha$ regions play a crucial role in shaping the motion and structure of the surrounding interstellar medium (Armentrout 2018). The left panel of Figure 6 provides a histogram of the angular distances between the peaks of HC_3N^* and $\text{H}40\alpha$ emission in sources associated with UC $\text{H}\alpha$ regions. In hot cores associated with UC $\text{H}\alpha$ regions separated by less than 4500 au, UV radiation has the potential to push interstellar molecules away from the cloud core due to radiation pressure. However, at larger separations, the peak shifts may be attributed to two factors. Firstly, photodissociation of HC_3N^* molecules occurs due to the radiation from UC $\text{H}\alpha$ regions. Secondly, molecular gas densities at peak positions of UC $\text{H}\alpha$ regions fall below the critical densities and HC_3N^* can not be effectively stimulated. These cases suggest that hot cores associated with UC $\text{H}\alpha$ regions might be influenced by an energy source distinct from the one driving the UC $\text{H}\alpha$ region itself. The right panel of Figure 6 displays a histogram of the angular distances between the peaks of HC_3N^* and continuum emission in sources without UC $\text{H}\alpha$ regions. In most hot cores without UC $\text{H}\alpha$ regions, where the peaks of HC_3N^* and continuum emissions are well-aligned, the heating source is likely stars (or protostars) with luminosities below 10^3 L_\odot , insufficient to generate an $\text{H}\alpha$ region through UV photon emission. This proposition is further supported by the observation that half of the cores listed in Table 3 have masses below 50 M_\odot , which is typically inadequate to form luminous protostars. In a few cases, hot cores may be heated by luminous protostars with strong UV radiation, but the appearance of an $\text{H}\alpha$ region is being quenched by the infalling gas.

We have categorized the types of hot core based on the number of HC_3N^* states, referring to each category as a different excitation type (e.g., Excitation type 2 means that a hot core has $\text{HC}_3\text{N} v_7=1$ and $v_7=2$ lines, and excitation type 3 means that a hot core has $\text{HC}_3\text{N} v_7=1$, $v_7=2$ and $v_6=1$ lines.). Figure 7 illustrates the correlation between integrated flux and peak flux of dust both associated with and without UC $\text{H}\alpha$ regions. After the

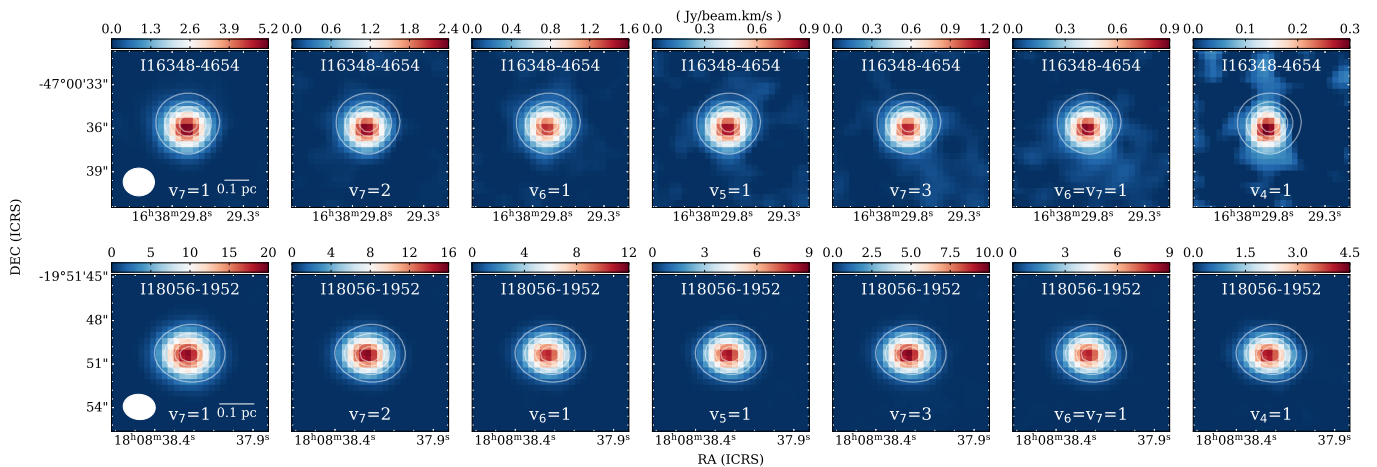


Fig. 3: Spatial distribution of 7 HC_3N^* lines of hot cores in IRAS 16348-4654 (top row) and IRAS 18056-1952 (bottom row). The background image of each panel from left to right is the moment 0 map of the (a) $v_7=1$, $E_u=349.77530$ K, (b) $v_7=2$, $E_u=670.68918$ & 673.96249 & 673.96308 K, (c) $v_6=1$, $E_u=746.53960$ K, $E_u=1065.29153$ & 1066.4191 K, (d) $v_5=1$ $E_u=983.03920$ K, (e) $v_7=3$, $E_u=990.39731$ K, (f) $v_6=v_7=1$, and (g) $v_4=1$, $E_u=1274.35207$ K emission. The white contours represent the intensity of continuum emission, with contour levels ranging from 10% to 90% of the peak values in steps of 20%. The corresponding beam sizes are shown in the bottom left corner and the linear scales are shown in the bottom right corner of the first image of each panel.

correction of continuum flux by deducting free-free emission, hot cores with higher energy levels of excitation types tend to have higher dust flux. The ratio of peak intensity to integrated intensity can indicate whether a source is compact or extended, with a higher ratio suggesting a more compact source. The hot cores with HC_3N^* excitation has a strong linear relationship between the peak dust flux and the integrated dust flux, indicating that these sources are relatively compact. In contrast, hot cores without HC_3N^* excitation or only with $v_7=1$ states have a poor linear relationship, suggesting that these hot cores are not dense enough. This suggests that the excitation of HC_3N^* requires a dense environment.

4.2. Differentiation of HC_3N^* column density

For excitation types 2 and 3, which have close upper energy levels, display similar HC_3N^* column densities, ranging from $(6.9 \pm 0.3) \times 10^{15}$ to $(2.5 \pm 0.1) \times 10^{16}$ cm^{-2} . Similarly, excitation types 5 and 6, also with comparable upper energy levels, have HC_3N^* column density values ranging from $(1.4 \pm 0.1) \times 10^{16}$ to $(7.6 \pm 0.1) \times 10^{16}$ cm^{-2} . In particular, the two hot cores classified as excitation type 7 exhibit the highest HC_3N^* column densities, exceeding 10^{17} cm^{-2} . Therefore, significant differences in HC_3N^* column density are observed between these various types of hot cores. Figure 8 illustrates the column densities for all types of hot cores possessing different numbers of HC_3N^* states. Obviously, The HC_3N^* column density generally increases with the increase of the upper energy level, and hot cores with similar upper energy levels exhibit similar HC_3N^* column densities.

Based on these excitation types, we identify two distinguishing values of HC_3N^* column density: 1.9×10^{16} cm^{-2} and 7.6×10^{16} cm^{-2} . For hot cores in excitation types 2 and 3, 92.3% have column densities below the first distinguishing value of 1.9×10^{16} cm^{-2} . In contrast, 92.9% of hot cores in excitation types 5 and 6 have column densities between the two distinguishing values, ranging from 1.9×10^{16} cm^{-2} to 7.6×10^{16} cm^{-2} . All hot cores in excitation type 7 have N_{H_2} exceeding the second distinguishing value of 7.6×10^{16} cm^{-2} . These observations indicate

that the number of vibrationally excited states increases with the overall column density of HC_3N^* .

4.3. Excitation factors

The excitation of HC_3N^* states can be produced by two different mechanisms: pumping by the absorption of mid-IR photons, and/or collisions with H_2 . The strong thermal emission by hot dust which provides high-energy mid-IR photons, can excite HC_3N^* from a low to a high energy level. The excitation of HC_3N^* states may also be impacted by the H_2 number density $n(\text{H}_2)$. When $n(\text{H}_2)$ exceeds n_{crit} for collision excitation of vibration levels, the excitation of a vibrationally excited state will be dominated by collisions with H_2 . Column 11 in table 3 to table 6 lists the $n(\text{H}_2)$ for all sources. Figure 9 illustrates the distribution of $n(\text{H}_2)$ as a function of upper level energy. All hot cores in our sample except for I18507+0110, with low $n(\text{H}_2)$ less than n_{crit} , indicating that excitation of HC_3N^* is dominated by mid-IR pumping and collisional excitation is relatively ineffective, in agreement with previous observations (Goldsmith et al. 1985; Schilke et al. 1992).

5. Conclusions

In this paper, we have performed a systematic survey of vibrational excited HC_3N lines (HC_3N^*) in hot cores, using the data of ALMA band 3 survey obtained by the ATOMS project. The main results are summarized as follows:

(1) Emission from 7 different HC_3N^* states has been detected in 52 out of the 60 hot cores. The detection rates for different HC_3N^* states decrease with increasing upper level energy. If a hot core has a high energy level line detected, then a low energy level line is invariably present.

(2) By analyzing the spatial distribution of HC_3N $v_7=1$ and UC HII regions, we found the spatial distribution of HC_3N^* is influenced by the presence of UC HII regions.

(3) The derived rotation temperature for HC_3N^* ranges from (160 ± 1) to (335 ± 2) K, with a mean value of 235 K, and the H_2 number density ranges from $(1.3 \pm 0.2) \times 10^5$ to $(5.0 \pm 0.5) \times 10^8$

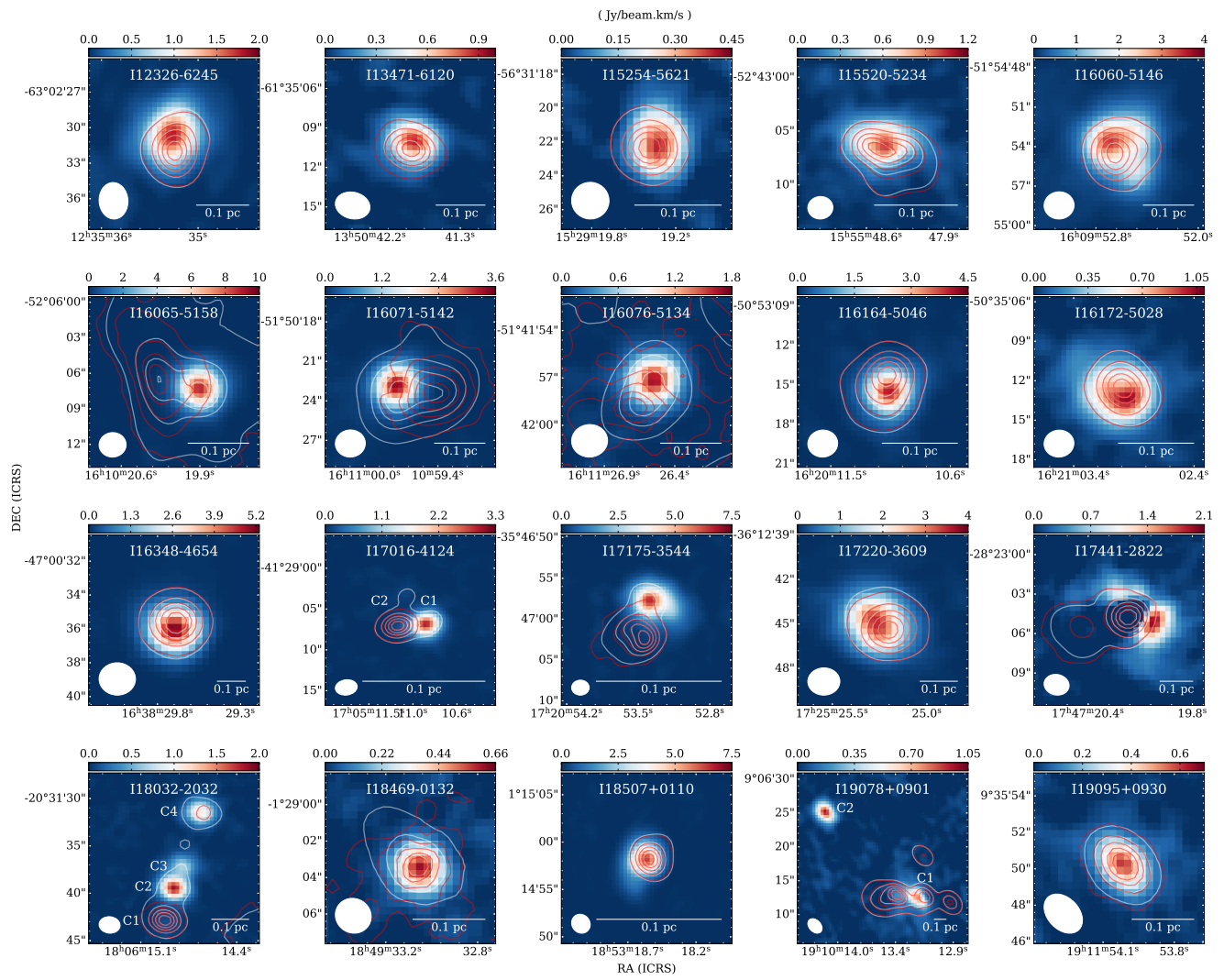


Fig. 4: Spatial distributions of HC_3N $v_7=1$ emission in 20 sources associated with UC HII regions. The background images are moment 0 maps of $v_7=1$ emission. The white contours represent the intensity of continuum emission, with contour levels ranging from 10% to 90% of the peak values in steps of 20%. The red contours represent the intensity of UC HII regions (traced by $\text{H}40\alpha$ emission), also with contour levels ranging from 10% to 90% of the peak values in steps of 20%. The corresponding beam sizes are shown in the bottom left corner and the linear scales are shown in the bottom right corner of the image of each source.

cm^{-3} , with a mean value of $3.2 \times 10^7 \text{ cm}^{-3}$. The high rotation temperature and substantial H_2 number density show that HC_3N^* excitation is from the inner region of hot cores.

(4) The column density of HC_3N^* ranges from $(6.9 \pm 0.3) \times 10^{15}$ to $(1.7 \pm 0.1) \times 10^{18} \text{ cm}^{-2}$, with a mean value of $2.7 \times 10^{16} \text{ cm}^{-2}$. Two distinguishing values of HC_3N^* column density for hot cores with different numbers of HC_3N^* states are obtained. Hot cores with less than four HC_3N^* states have a column density of less than $1.9 \times 10^{16} \text{ cm}^{-2}$, while those with more than six HC_3N^* states have a column density greater than $7.6 \times 10^{16} \text{ cm}^{-2}$. The column density of the remaining hot cores falls between these two values.

(5) In hot cores, the HC_3N^* states are pumped by the absorption of mid-IR photon rather than collisional excitation.

Acknowledgements. This work has been supported by the National Key R&D Program of China (No. 2022YFA1603100), the National Natural Science Foundation of China (NSFC) through grant Nos. 12033005, 12073061, and 12122307, and the Tianchi Talent Program of Xinjiang Uygur Autonomous Region. This research was carried out in part at the Jet Propulsion Laboratory, California Institute of Technology, under a contract with the National Aeronautics

and Space Administration (80NM0018D0004). G.G. gratefully acknowledges support by the ANID BASAL project FB210003. M.Y.T. acknowledges the support by the NSFC through grant No. 12203011, and the Yunnan Provincial Department of Science and Technology through grant No. 202101BA070001-261. PS was partially supported by a Grant-in-Aid for Scientific Research (KAKENHI Number JP22H01271 and JP23H01221) of JSPS. PS was supported by Yoshinori Ohsumi Fund (Yoshinori Ohsumi Award for Fundamental Research). SRD acknowledges support from the Fondecyt Postdoctoral fellowship (project code 3220162) and ANID BASAL project FB210003. LB gratefully acknowledges support by the ANID BASAL project FB210003. CWL was supported by the Basic Science Research Program through the NRF funded by the Ministry of Education, Science and Technology (NRF- 2019R1A2C1010851) and by the Korea Astronomy and Space Science Institute grant funded by the Korea government (MSIT; project No. 2024-1-841-00). H.-L. Liu was supported by Yunnan Fundamental Research Project (grant Nos 202301AT070118, and 202401AS070121), and by Xingdian Talent Support Plan Youth Project. X.H.L. acknowledges support from the Natural Science Foundation of Xinjiang Uygur Autonomous Region (No. 2024D01E37) and the National Science Foundation of China (12473025). This work is sponsored in part by the Chinese Academy of Sciences (CAS), through a grant to the CAS South America Center for Astronomy (CASSACA) in Santiago, Chile. This paper makes use of the following ALMA data: ADS/JAO.ALMA#2019.1.00685.S. ALMA is a partnership of ESO (representing its member states), NSF (USA), and NINS (Japan), together with NRC (Canada), MOST and ASIAA (Taiwan), and KASI (Republic of Korea), in

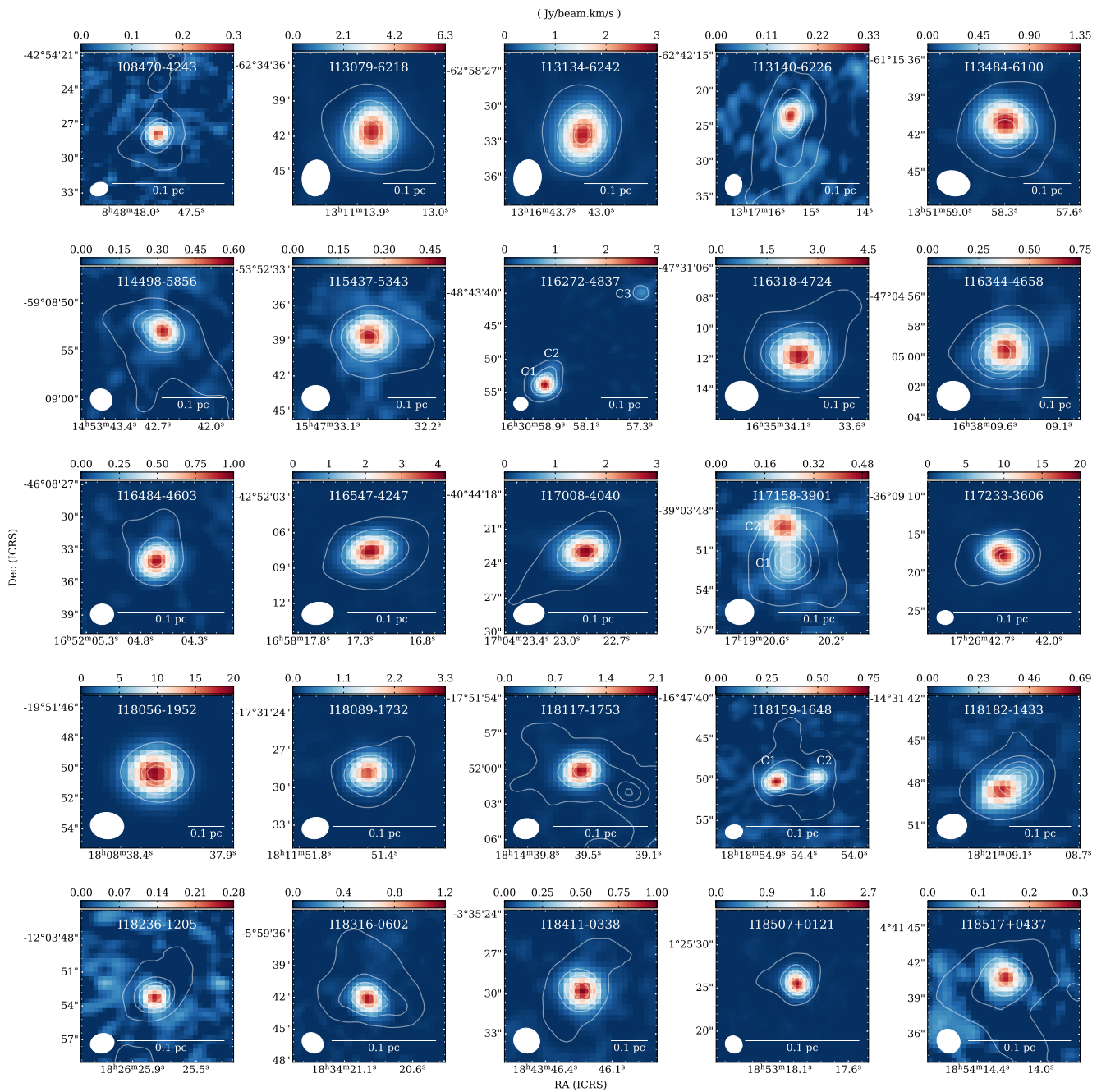


Fig. 5: Spatial distribution of HC_3N $v_7=1$ in 25 sources without UC H α regions. The background images are moment 0 maps of $v_7=1$ emissions. The white contours represent the intensity of continuum emission, with contour levels ranging from 10% to 90% of the peak values in steps of 20%. The corresponding beam sizes are shown in the bottom left corner and the linear scales are shown in the bottom right corner of the image of each source.

cooperation with the Republic of Chile. The Joint ALMA Observatory is operated by ESO, AUI/NRAO, and NAOJ.

Software

This work has made use of the following software: CASA (McMullin et al. 2007; CASA Team et al. 2022), XCLASS (Möller et al. 2017), MAGIX (Möller et al. 2013).

References

- Afflerbach, A., Churchwell, E., Acord, J. M., et al. 1996, ApJS, 106, 423
- Armentrout, W. P. 2018, PhD thesis, West Virginia University
- Belloche, A., Müller, H. S. P., Menten, K. M., Schilke, P., & Comito, C. 2013, A&A, 559, A47
- Bergin, E. A., Snell, R. L., & Goldsmith, P. F. 1996, ApJ, 460, 343

Facilities

This work has made use of the following facility: ALMA

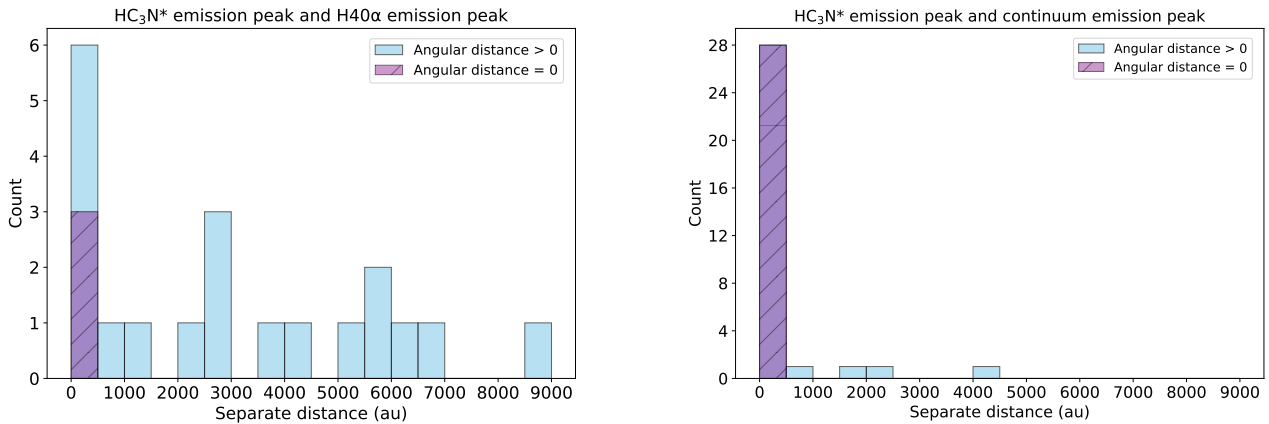


Fig. 6: Histogram of the separations (angular distances) between the peak of the HC₃N* emission and peak of the continuum emission for sources without UC HII regions (left panel) and the separations between the peak of the HC₃N* emission and peak of the H40 α emission for sources associated with UC HII regions (right panel). The blue bars represent sources with angular distances greater than 0, and the purple bars represent sources with angular distances equal to 0.

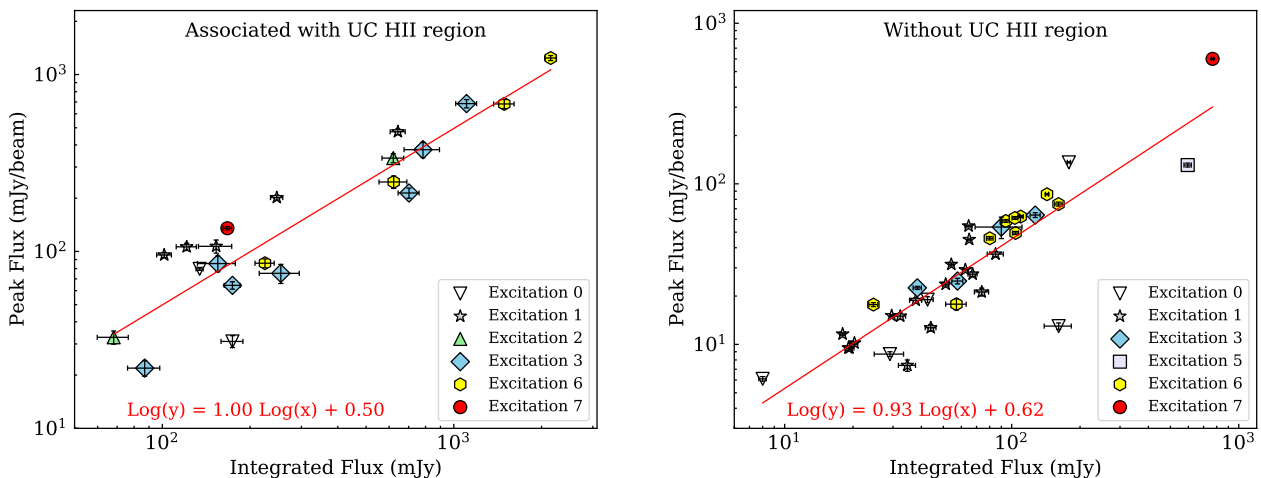


Fig. 7: Scatter plot of peak flux versus integrated flux for sources associated with UC HII regions (left panel) and for sources without UC HII regions (right panel). Different markers represent different types of hot cores which possess different numbers of HC₃N* states. The linear least-squares fit for all dots is shown as a red solid line.

- Bonfand, M., Belloche, A., Garrod, R. T., et al. 2019, A&A, 628, A27
 Bonfand, M., Csengeri, T., Bontemps, S., et al. 2024, A&A, 687, A163
 CASA Team, Bean, B., Bhatnagar, S., et al. 2022, PASP, 134, 114501
 Chung, H. S., Osamu, K., & Masaki, M. 1991, Journal of Korean Astronomical Society, 24, 217
 Churchwell, E. 2002, ARA&A, 40, 27
 Condon, J. J. & Ransom, S. M. 2016, Essential Radio Astronomy
 Costagliola, F. & Aalto, S. 2010, A&A, 515, A71
 de Vicente, P., Martín-Pintado, J., Neri, R., & Colom, P. 2000, A&A, 361, 1058
 Endres, C. P., Schlemmer, S., Schilke, P., Stutzki, J., & Müller, H. S. P. 2016, Journal of Molecular Spectroscopy, 327, 95
 Esplugues, G. B., Cernicharo, J., Viti, S., et al. 2013, A&A, 559, A51
 Frau, P., Girart, J. M., Beltrán, M. T., et al. 2010, ApJ, 723, 1665
 Gerin, M., Neufeld, D. A., & Goicoechea, J. R. 2016, ARA&A, 54, 181
 Giannetti, A., Leurini, S., König, C., et al. 2017, A&A, 606, L12
 Goldsmith, P. F., Krotkov, R., & Snell, R. L. 1985, ApJ, 299, 405
 Goldsmith, P. F. & Langer, W. D. 1999, ApJ, 517, 209
 Goldsmith, P. F., Snell, R. L., Deguchi, S., Krotkov, R., & Linke, R. A. 1982, ApJ, 260, 147
 He, Y.-X., Henkel, C., Zhou, J.-J., et al. 2021, ApJS, 253, 2
 Herbst, E. & van Dishoeck, E. F. 2009, ARA&A, 47, 427
 Hildebrand, R. H. 1983, QJRAS, 24, 267
 Jørgensen, J. K., Belloche, A., & Garrod, R. T. 2020, ARA&A, 58, 727
 Kauffmann, J., Bertoldi, F., Bourke, T. L., Evans, N. J., I., & Lee, C. W. 2008, A&A, 487, 993
 Khan, S., Pandian, J. D., Lal, D. V., et al. 2022, A&A, 664, A140
 Kunde, V. G., Aikin, A. C., Hanel, R. A., et al. 1981, Nature, 292, 686
 Leach, S., Garcia, G. A., Mahjoub, A., et al. 2014, J. Chem. Phys., 140, 174305
 Li, D. & Goldsmith, P. F. 2012, ApJ, 756, 12
 Li, S., Wang, J., Zhang, Z.-Y., et al. 2017, MNRAS, 466, 248
 Liu, H.-L., Liu, T., Evans, Neal J., I., et al. 2021, MNRAS, 505, 2801
 Liu, T., Evans, N. J., Kim, K.-T., et al. 2020, MNRAS, 496, 2790
 Liu, X., Liu, T., Shen, Z., et al. 2024, ApJS, 271, 3
 Lu, X., Cheng, Y., Ginsburg, A., et al. 2020, ApJ, 894, L14
 Luo, A.-X., Liu, H.-L., Li, G.-X., Pan, S., & Yang, D.-T. 2024, Research in Astronomy and Astrophysics, 24, 065003
 Mallinson, P. D. & Fayt, A. 1976, Molecular Physics, 32, 473
 Martín, S., Mangum, J. G., Harada, N., et al. 2021, A&A, 656, A46
 Mauersberger, R., Henkel, C., & Sage, L. J. 1990, A&A, 236, 63
 McMullin, J. P., Waters, B., Schiebel, D., Young, W., & Golap, K. 2007, in Astronomical Society of the Pacific Conference Series, Vol. 376, Astronomical Data Analysis Software and Systems XVI, ed. R. A. Shaw, F. Hill, & D. J. Bell, 127

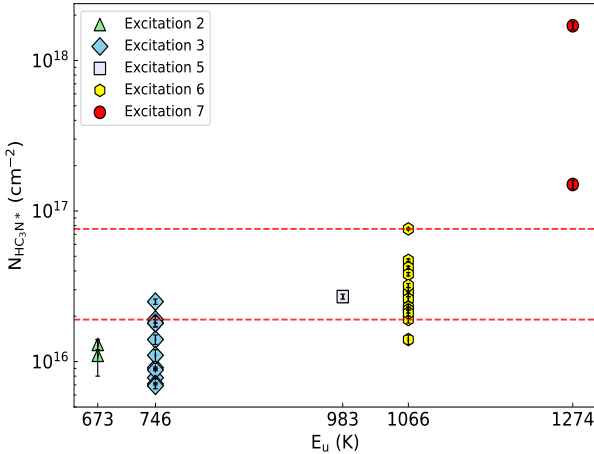


Fig. 8: Scatter plot of the distribution of HC_3N^* column density as a function of upper level energy. Different markers represent different types of hot cores which possess different numbers of HC_3N^* emission lines. The two horizontal dashed red lines represent the two distinguishing values for the column density of $1.9 \times 10^{16} \text{ cm}^{-2}$ and $7.6 \times 10^{16} \text{ cm}^{-2}$, respectively.

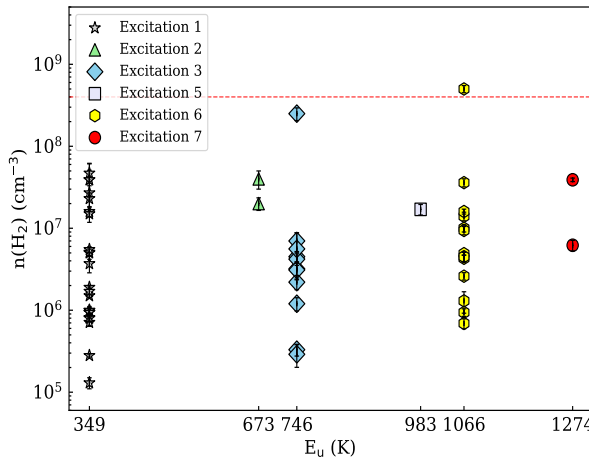


Fig. 9: Scatter plot of the distribution of H_2 number density as a function of upper level energy. Different markers represent different types of hot cores which possess different numbers of HC_3N^* emission lines. The horizontal dashed red line represents the critical density of $4 \times 10^8 \text{ cm}^{-3}$ for $\text{HC}_3\text{N} v_7=1$ excitation.

- Möller, T., Bernst, I., Panoglou, D., et al. 2013, MAGIX: Modeling and Analysis Generic Interface for eXternal numerical codes, Astrophysics Source Code Library, record ascl:1303.009
 Möller, T., Endres, C., & Schilke, P. 2017, A&A, 598, A7
 Motte, F., Bontemps, S., & Louvet, F. 2018, ARA&A, 56, 41
 Müller, H. S. P., Schlöder, F., Stutzki, J., & Winnewisser, G. 2005, Journal of Molecular Structure, 742, 215
 Müller, H. S. P., Thorwirth, S., Roth, D. A., & Winnewisser, G. 2001, A&A, 370, L49
 Ossenkopf, V., & Henning, T. 1994, A&A, 291, 943
 Pagani, L., Favre, C., Goldsmith, P. F., et al. 2017, A&A, 604, A32
 Peng, Y., Qin, S.-L., Schilke, P., et al. 2017, ApJ, 837, 49
 Pickett, H. M., Poynter, R. L., Cohen, E. A., et al. 1998, J. Quant. Spectr. Rad. Transf., 60, 883

- Qin, S.-L., Liu, T., Liu, X., et al. 2022, MNRAS, 511, 3463
 Ranković, M., Nag, P., Zawadzki, M., et al. 2018, Phys. Rev. A, 98, 052708
 Rico-Villas, F., Martín-Pintado, J., González-Alfonso, E., Martín, S., & Rivilla, V. M. 2020, MNRAS, 491, 4573
 Rico-Villas, F., Martín-Pintado, J., González-Alfonso, E., et al. 2021, MNRAS, 502, 3021
 Rosen, A. L. 2022, ApJ, 941, 202
 Saha, A., Tej, A., Liu, H.-L., et al. 2022, MNRAS, 516, 1983
 Schilke, P., Guesten, R., Schulz, A., Serabyn, E., & Walmsley, C. M. 1992, A&A, 261, L5
 Shaver, P. A. 1970, Astrophys. Lett., 5, 167
 Tang, M., Liu, T., Qin, S.-L., et al. 2018, ApJ, 856, 141
 Taniguchi, K., Saito, M., Sridharan, T. K., & Minamidani, T. 2018, ApJ, 854, 133
 Taniguchi, K., Sanhueza, P., Olguin, F. A., et al. 2023, ApJ, 950, 57
 Taniguchi, K., Tanaka, K. E. I., Zhang, Y., et al. 2022, ApJ, 931, 99
 Turner, B. E. 1971, ApJ, 163, L35
 van Dishoeck, E. F. 2018, in IAU Symposium, Vol. 332, Astrochemistry VII: Through the Cosmos from Galaxies to Planets, ed. M. Cunningham, T. Millar, & Y. Aikawa, 3–22
 Velilla Prieto, L., Sánchez Contreras, C., Cernicharo, J., et al. 2015, A&A, 575, A84
 Wang, J., Li, D., Goldsmith, P. F., et al. 2020, ApJ, 889, 129
 Wyrowski, F., Schilke, P., & Walmsley, C. M. 1999, A&A, 341, 882
 Yu, N., Wang, J.-J., & Xu, J.-L. 2019, MNRAS, 489, 4497
 Yue, Y.-H., Qin, S.-L., Liu, T., et al. 2021, Research in Astronomy and Astrophysics, 21, 014
 Zhang, C.-P. & Li, G.-X. 2017, MNRAS, 469, 2286
 Zinchenko, I. I., Dewangan, L. K., Baug, T., Ojha, D. K., & Bhadari, N. K. 2021, MNRAS, 506, L45

¹ School of Physics and Astronomy, Yunnan University, Kunming 650091, People's Republic of China
 e-mail: li.chen@mail.ynu.edu.cn, qin@ynu.edu.cn

² Shanghai Astronomical Observatory, Chinese Academy of Sciences, 80 Nandan Road, Shanghai 200030, People's Republic of China
 e-mail: liutie@shao.ac.cn

³ Jet Propulsion Laboratory, California Institute of Technology, 4800 Oak Grove Drive, Pasadena CA 91109, USA

⁴ Department of Physics, Faculty of Science, Kunming University of Science and Technology, Kunming 650500, People's Republic of China

⁵ Xinjiang Astronomical Observatory, Chinese Academy of Sciences, 150 Science 1-Stree, Urumqi, Xinjiang 830011, People's Republic of China

⁶ Xinjiang Key Laboratory of Radio Astrophysics, 150 Science 1-Street, Urumqi, Xinjiang 830011, People's Republic of China

⁷ Departamento de Astronomía, Universidad de Chile, Las Condes, 7591245 Santiago, Chile

⁸ Chinese Academy of Sciences South America Center for Astronomy, National Astronomical Observatories, CAS, Beijing 100101, People's Republic of China

⁹ University of Chinese Academy of Sciences, Beijing 100049, People's Republic of China

¹⁰ Institute of Astrophysics, School of Physics and Electronical Science, Chuxiong Normal University, Chuxiong 675000, People's Republic of China

¹¹ Department of Earth and Planetary Sciences, Institute of Science Tokyo, Meguro, Tokyo, 152-8551, Japan

¹² National Astronomical Observatory of Japan, National Institutes of Natural Sciences, 2-21-1 Osawa, Mitaka, Tokyo 181-8588, Japan

¹³ Department of Astronomical Science, SOKENDAI (The Graduate University for Advanced Studies), 2-21-1 Osawa, Mitaka, Tokyo 181-8588, Japan

¹⁴ Rosseland Centre for Solar Physics, University of Oslo, PO Box 1029 Blindern, 0315 Oslo, Norway

¹⁵ Institute of Theoretical Astrophysics, University of Oslo, PO Box 1029 Blindern, 0315 Oslo, Norway

¹⁶ Physical Research Laboratory, Navrangpura, Ahmedabad 380 009, India

¹⁷ Instituto de Astronomía, Universidad Católica del Norte, Antofagasta, Chile

- ¹⁸ Max Planck Institute for Astronomy, Königstuhl 17, D-69117 Heidelberg, Germany
- ¹⁹ Korea Astronomy and Space Science Institute, 776 Daedeokdaero, Yuseong-gu, Daejeon 34055, Republic of Korea
- ²⁰ University of Science and Technology, Korea (UST), 217 Gajeong-ro, Yuseong-gu, Daejeon 34113, Republic of Korea
- ²¹ Department of Astronomy, Eötvös Loránd University, Pázmány Péter sétány 1/A, H-1117, Budapest, Hungary
- ²² University of Debrecen, Faculty of Science and Technology, Egyetemtér 1, H-4032 Debrecen, Hungary;
- ²³ Department of Mathematical Sciences, University of South Africa, Cnr Christian de Wet Rd and Pioneer Avenue, Florida Park, 1709 Roodepoort, South Africa
- ²⁴ Centre for Space Research, North-West University, Potchefstroom Campus, Private Bag X6001, Potchefstroom 2520, South Africa
- ²⁵ Department of Physics and Astronomy, Faculty of Physical Sciences, University of Nigeria, Carver Building, 1 University Road, Nsukka 410001, Nigeria
- ²⁶ I. Physikalisches Institut, Universität zu Köln, Zülpicher Straße 77, 50937 Köln, Germany
- ²⁷ Kavli Institute for Astronomy and Astrophysics, Peking University, 5 Yiheyuan Road, Haidian District, Beijing 100871, China
- ²⁸ School of Physics and Astronomy, Sun Yat-sen University, 2 Daxue Road, Zhuhai, Guangdong 519082, People's Republic of China

Appendix A: Parameters of vibrationally excited HC_3N lines in SPW 8.

Table A.1: Parameters of vibrationally excited HC_3N lines.

State	Frequency (MHz)	Uncertainty (MHz)	$J_{\text{up}} - J_{\text{low}}$	Parity	$S_{ij}\mu^2$ (D^2)	$\log_{10}(A_{ij})$ (s^{-1})	E_u (K)
$v_4=1$	99938.6314	0.0040	$J = 11 - 10$	–	147.65946	-4.12733	1274.35207
$v_5=1$	100085.1370	0.0055	$J = 11 - 10$	$1e$	150.47652	-4.11721	983.02211
$v_5=1$	100141.3008	0.0036	$J = 11 - 10$	$1f$	150.47652	-4.11647	983.03920
$v_6=1$	100240.5843	0.0016	$J = 11 - 10$	$1e$	151.47591	-4.11232	746.53960
$v_6=1$	100319.3816	0.0016	$J = 11 - 10$	$1f$	151.45767	-4.11135	746.56237
$v_7=1$	100322.4109	0.0017	$J = 11 - 10$	$1e$	151.18087	-4.11210	349.73387
$v_7=1$	100466.1745	0.0017	$J = 11 - 10$	$1f$	151.14994	-4.11033	349.77530
$v_6=v_7=1$	100593.4944	0.0030	$J = 11 - 10$	0^+	151.98949	-4.10627	1065.29153
$v_6=v_7=1$	100596.2397	0.0032	$J = 11 - 10$	0^-	151.95748	-4.10633	1066.4191
$v_6=v_7=1$	100604.0227	0.0024	$J = 11 - 10$	2^-	146.97639	-4.12070	1066.62147
$v_6=v_7=1$	100606.2047	0.0026	$J = 11 - 10$	2^+	146.97012	-4.12069	1066.62172
$v_7=2$	100708.7840	0.0020	$J = 11 - 10$	0	151.73124	-4.10552	670.68918
$v_7=2$	100711.0640	0.0015	$J = 11 - 10$	$2e$	146.72153	-4.12007	673.96249
$v_7=2$	100714.3951	0.0016	$J = 11 - 10$	$2f$	146.71208	-4.12005	673.96308
$v_7=3$	100880.5889	0.0049	$J = 11 - 10$	$1e$	149.75614	-4.10899	983.88413
$v_7=3$	101027.8491	0.0031	$J = 11 - 10$	3	139.77879	-4.13703	990.39731
$v_7=3$	101027.8709	0.0031	$J = 11 - 10$	3	139.77873	-4.13703	990.39731
$v_7=3$	101169.9207	0.0040	$J = 11 - 10$	$1f$	149.72959	-4.10533	983.96751

NOTE. The rest frequencies for all states are listed with uncertainties, and all transitions have the same $J = 11 - 10$.

Appendix B: Spectra of vibrationally excited HC_3N lines in SPW 8

In the survey observations, we detected a total of 7 types of HC_3N^* lines in 52 hot cores, comprising 18 transitions in SPW 8, with none detected in SPW 7, all corresponding to the same $J=11-10$ transition. Of the 52 hot cores, 29 show more than one HC_3N^* state, and we performed XCLASS fitting on the spectral lines. In Figure B.1, we labeled all detected HC_3N^* transitions and one HC_3N $v=0$ ground state transition.

Appendix C: Rotational Temperature Diagram

Figure C.1 presents the RTD analysis for 29 hot cores. Since XCLASS considers the effect of optical depth on line flux, while our RTD calculations do not apply this correction, the rotation temperature derived from RTD is unreliable for optically thick sources. Of these 29 hot cores, only IRAS 18056–1952 is optically thick. For the remaining 28 hot cores, the rotation temperatures obtained from XCLASS and RTD are consistent when considering the errors.

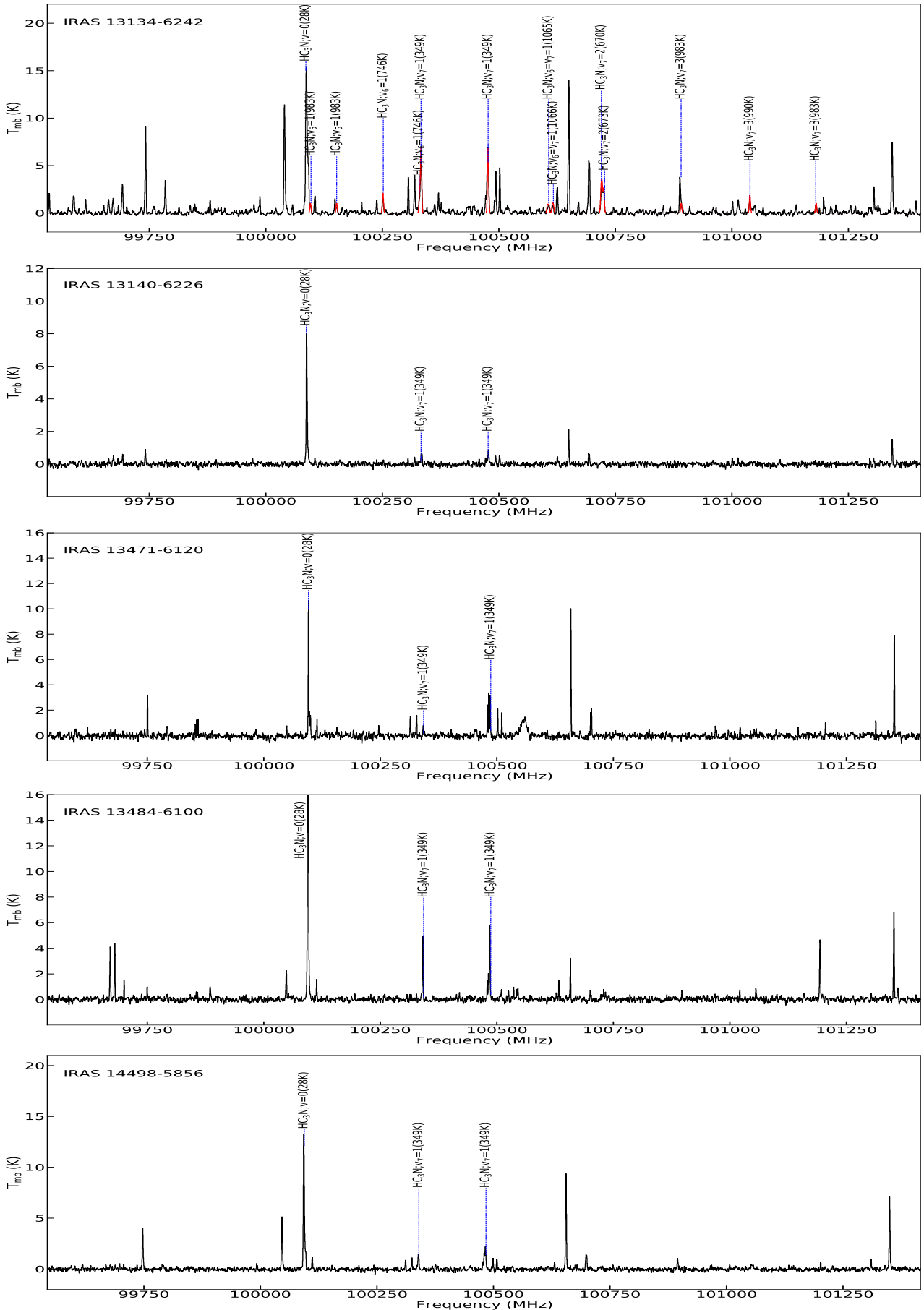


Fig. B.1: Spectra of HC_3N vibrationally excited lines for 52 hot cores. The black lines represent the observed spectra at sky frequency, while the red lines display the synthetic spectra based on the best-fitting parameters for the HC_3N^* lines.

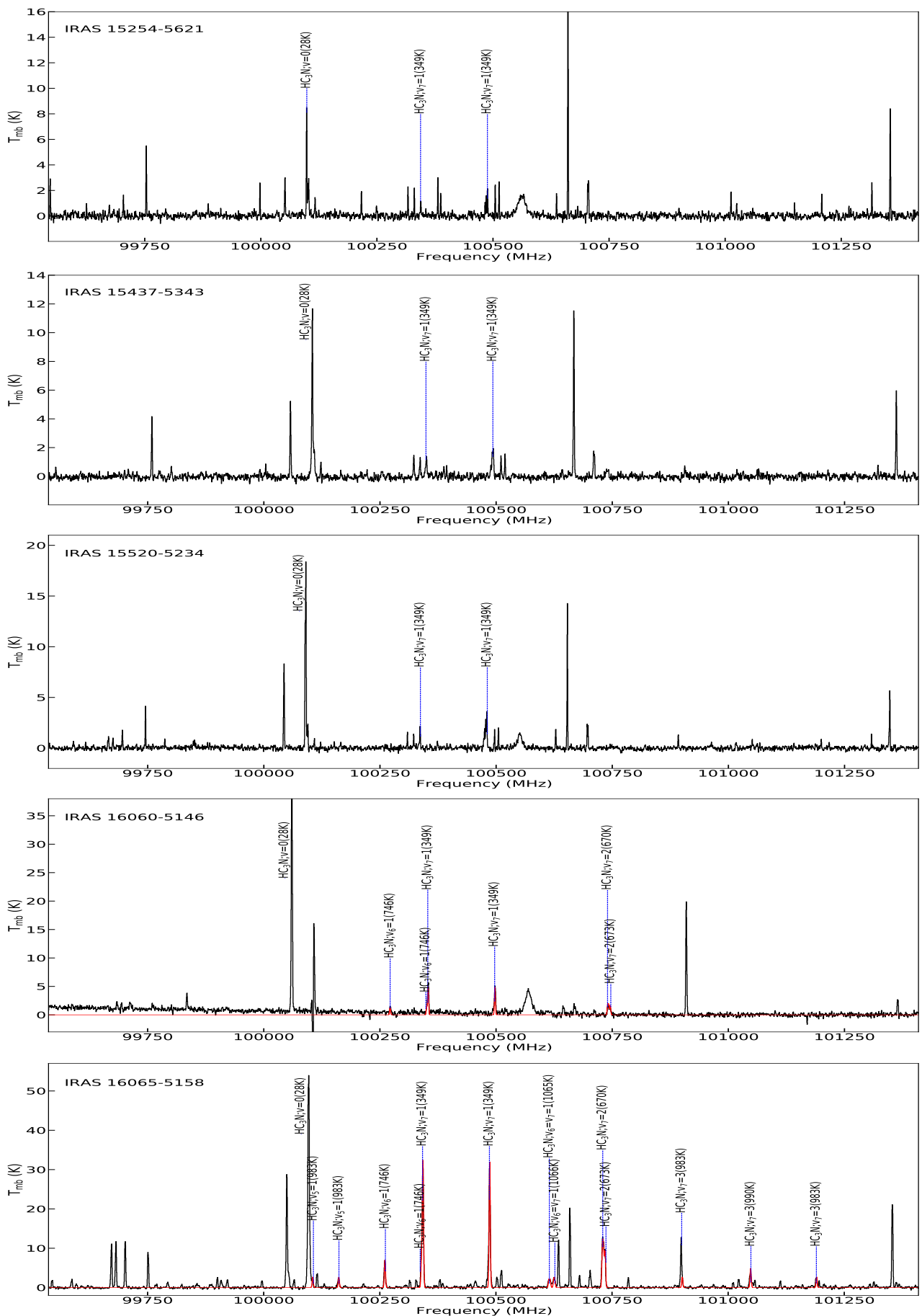


Fig. B.1: (continued.)

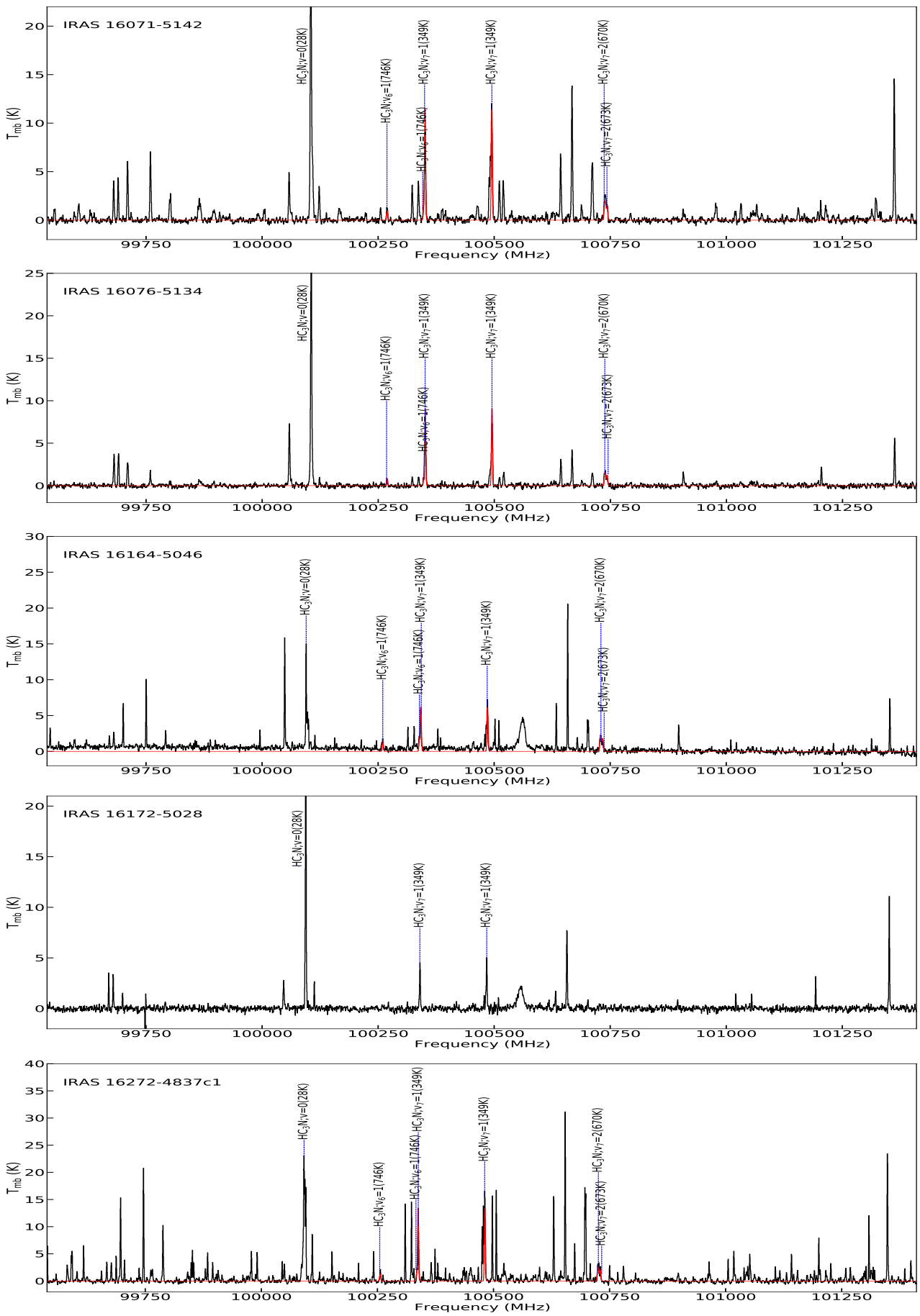


Fig. B.1: (continued.)

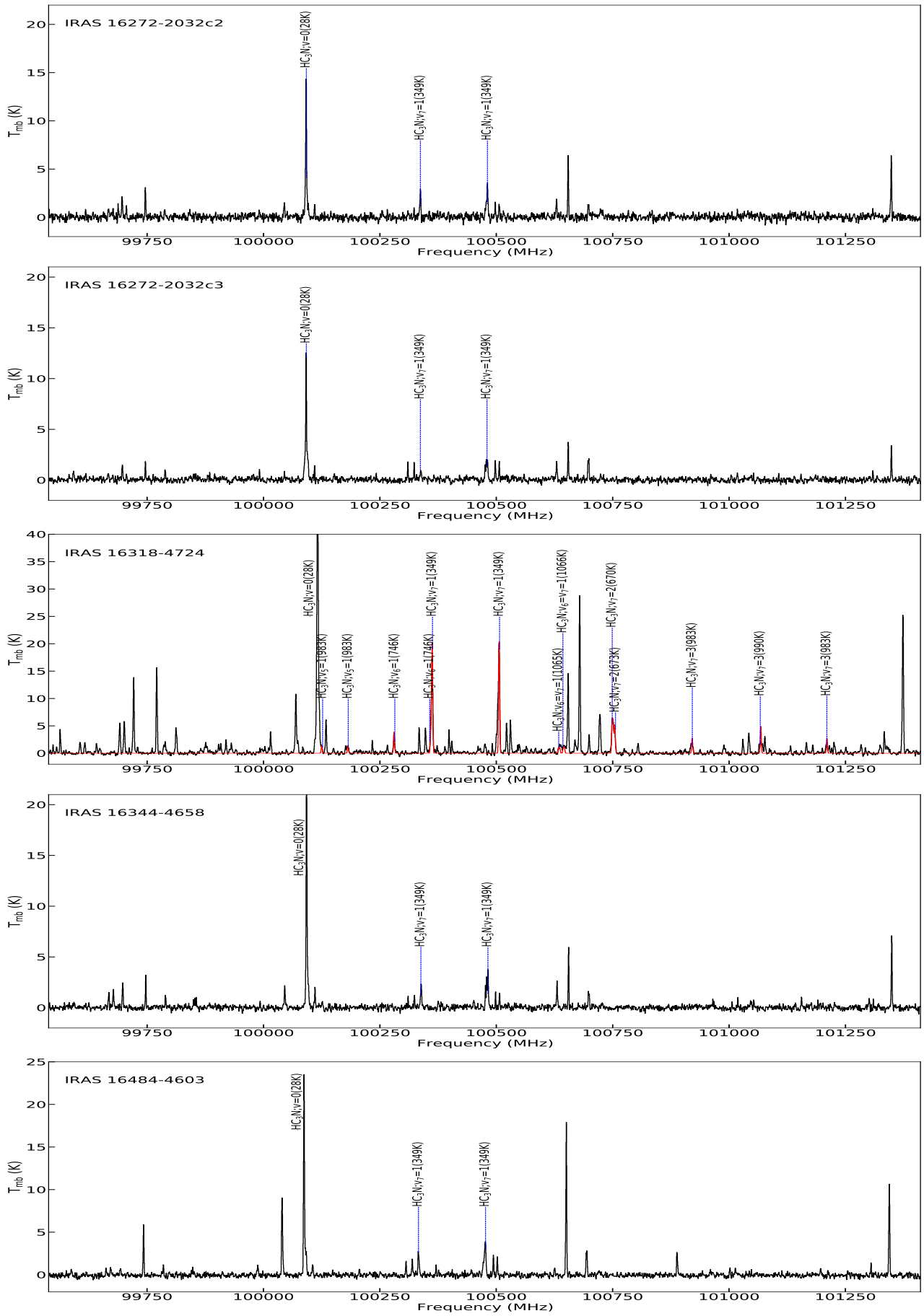


Fig. B.1: (continued.)

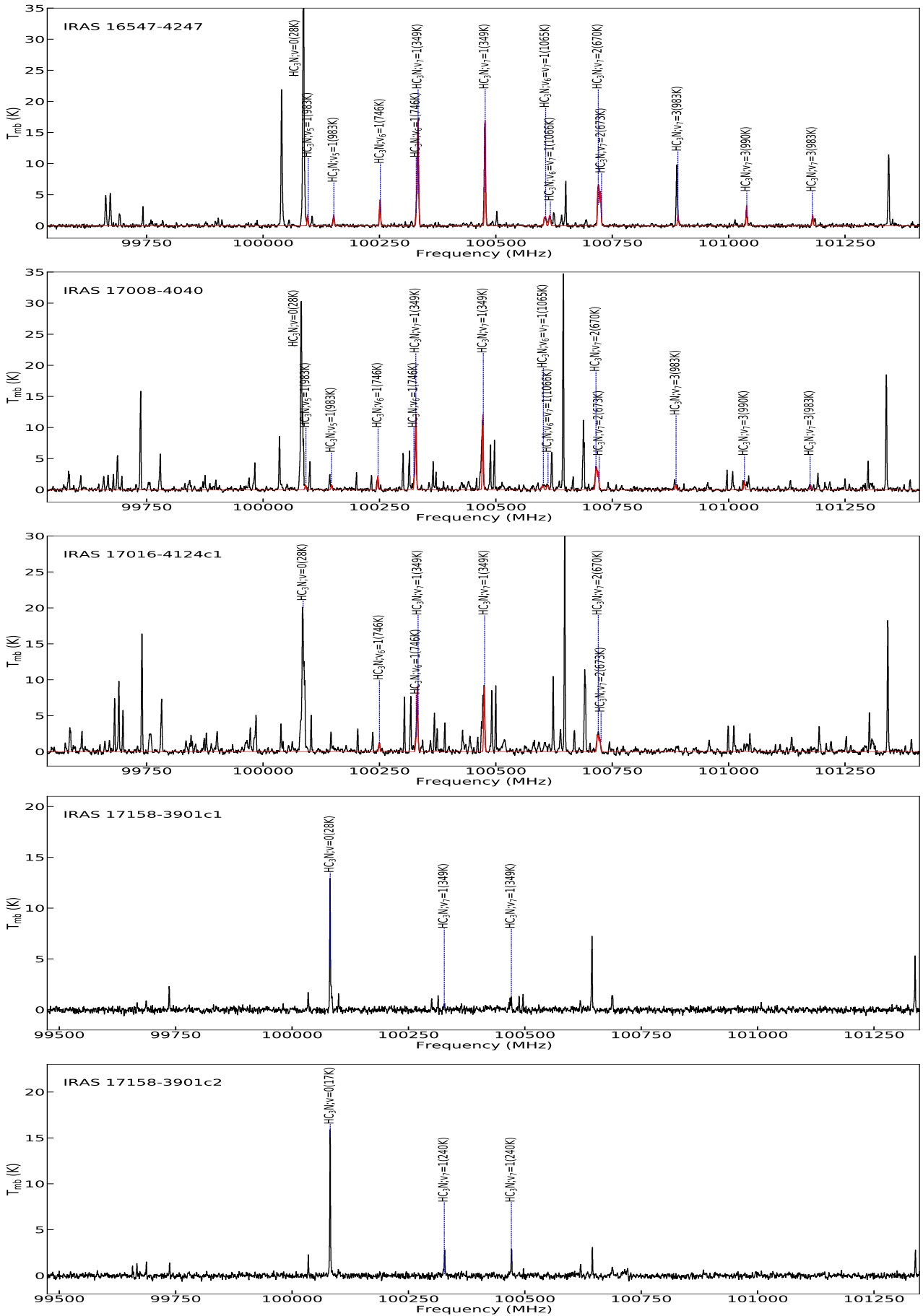


Fig. B.1: (continued.)

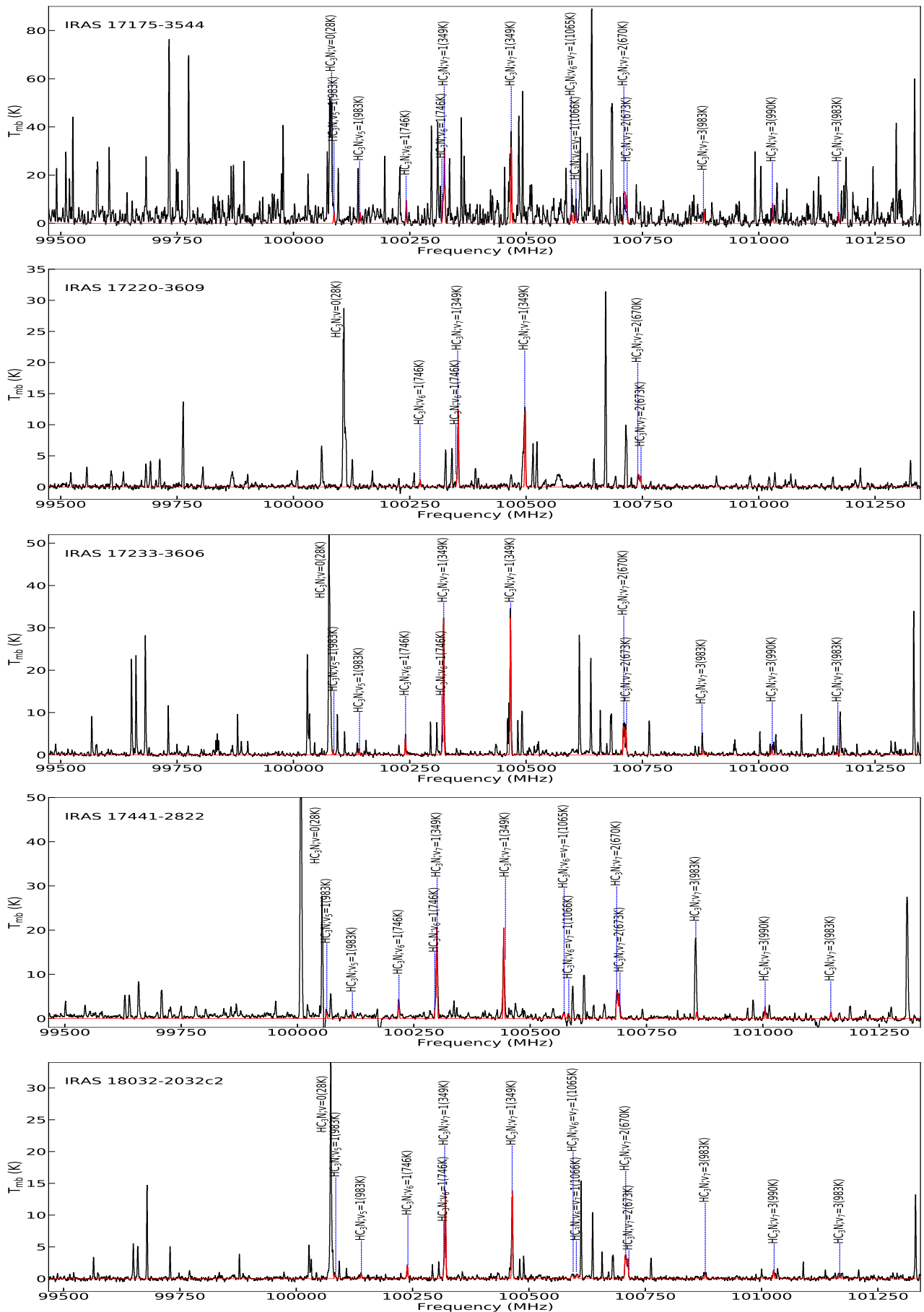


Fig. B.1: (continued.)

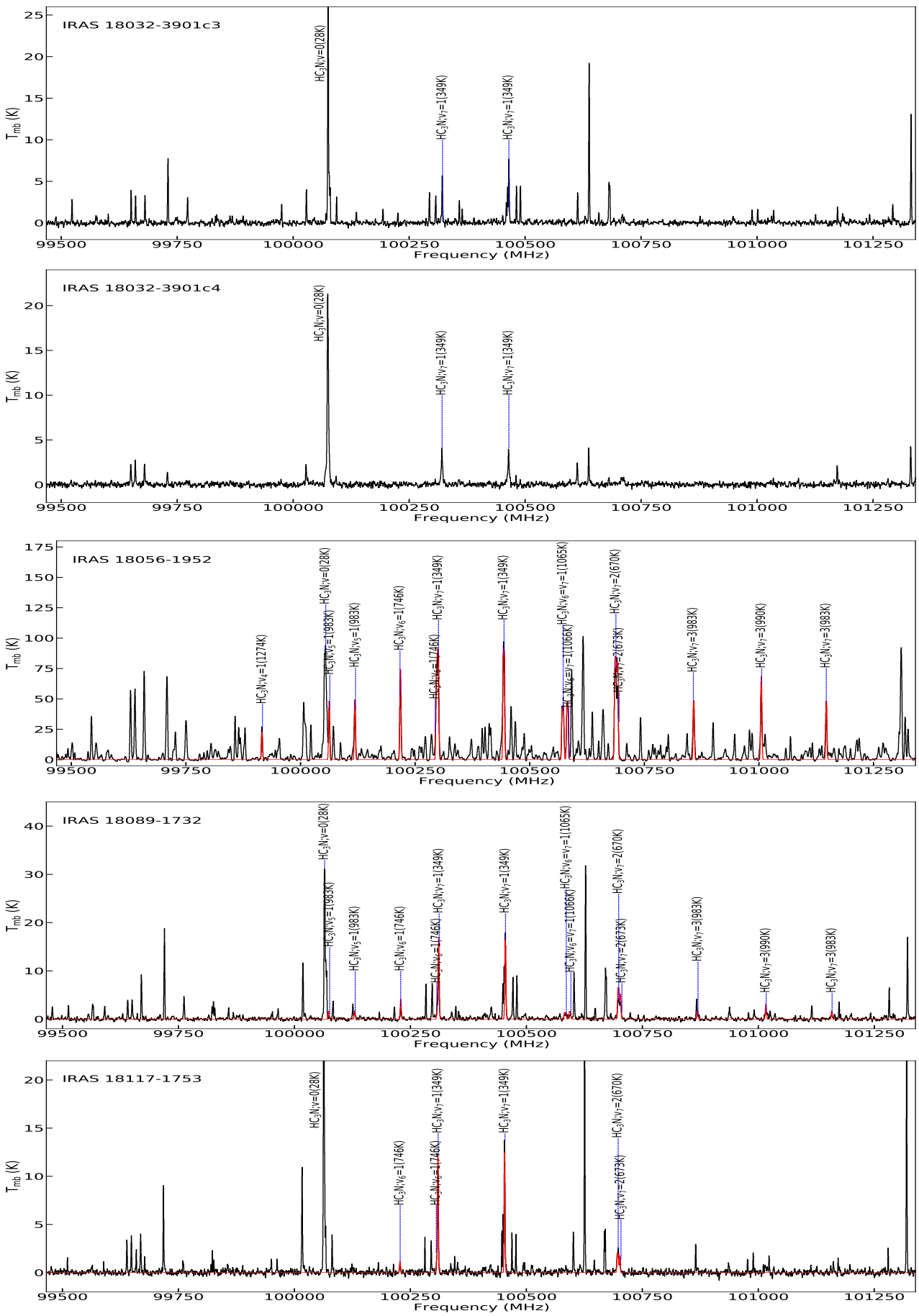


Fig. B.1: (continued.)

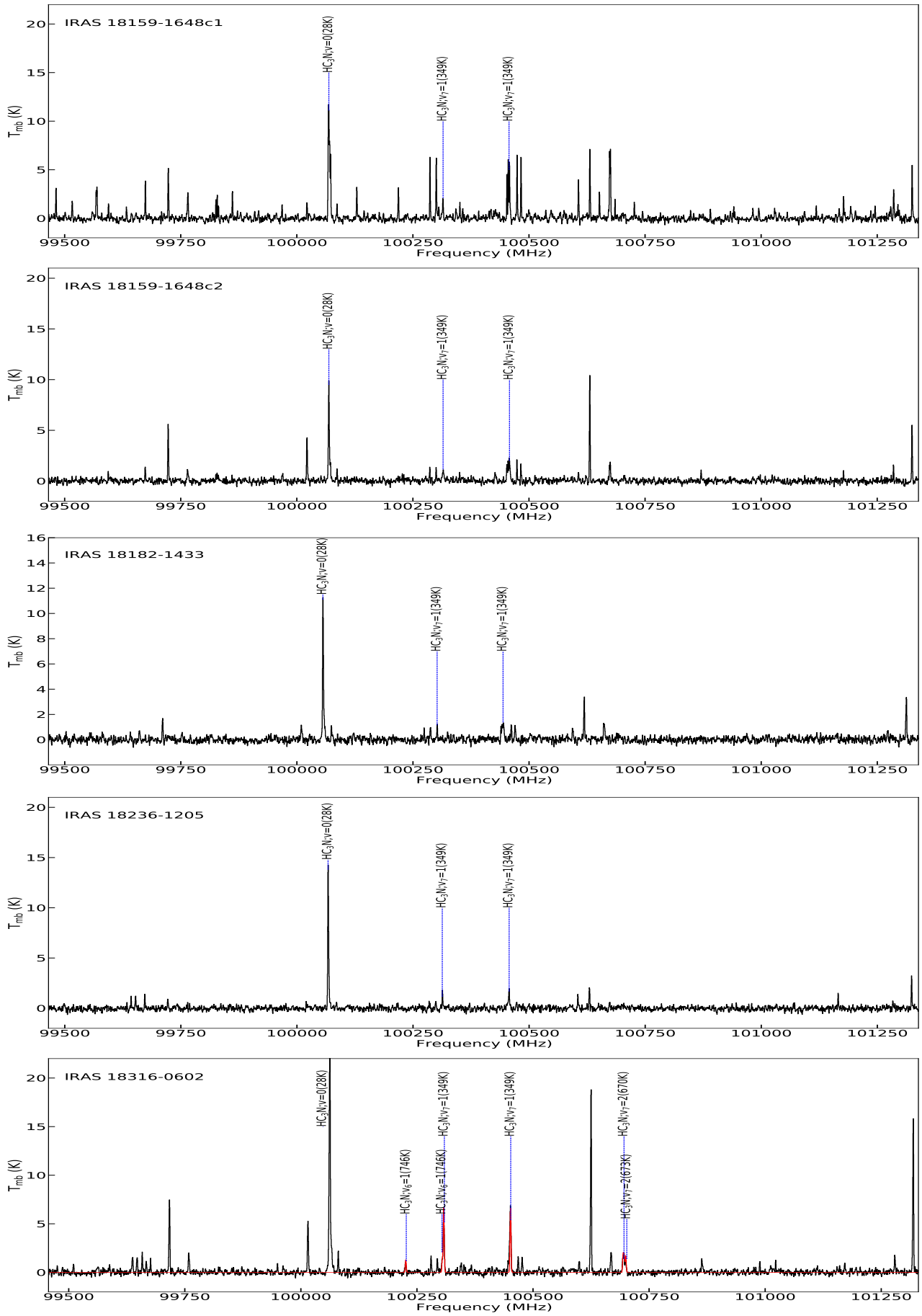
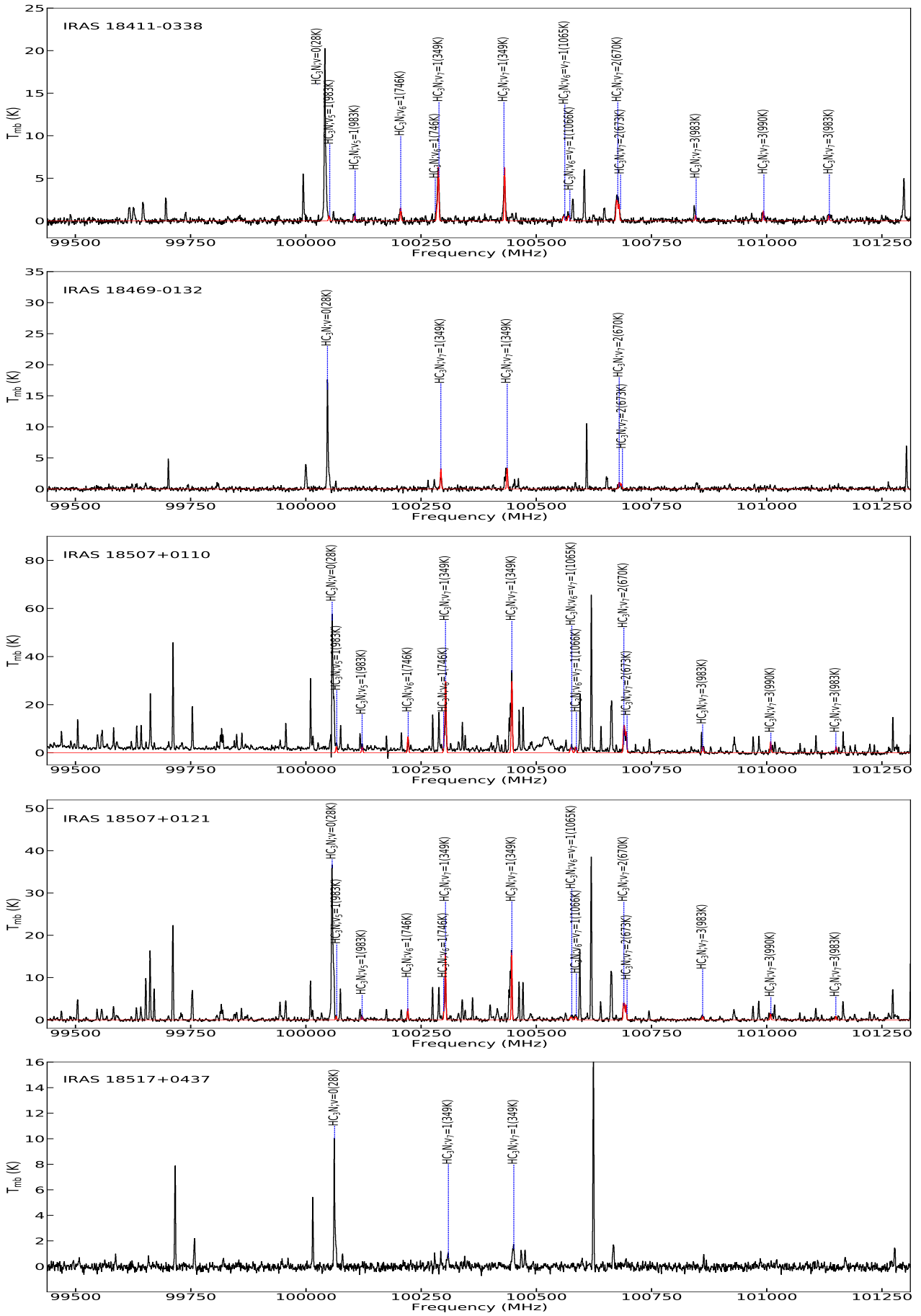


Fig. B.1: (continued.)



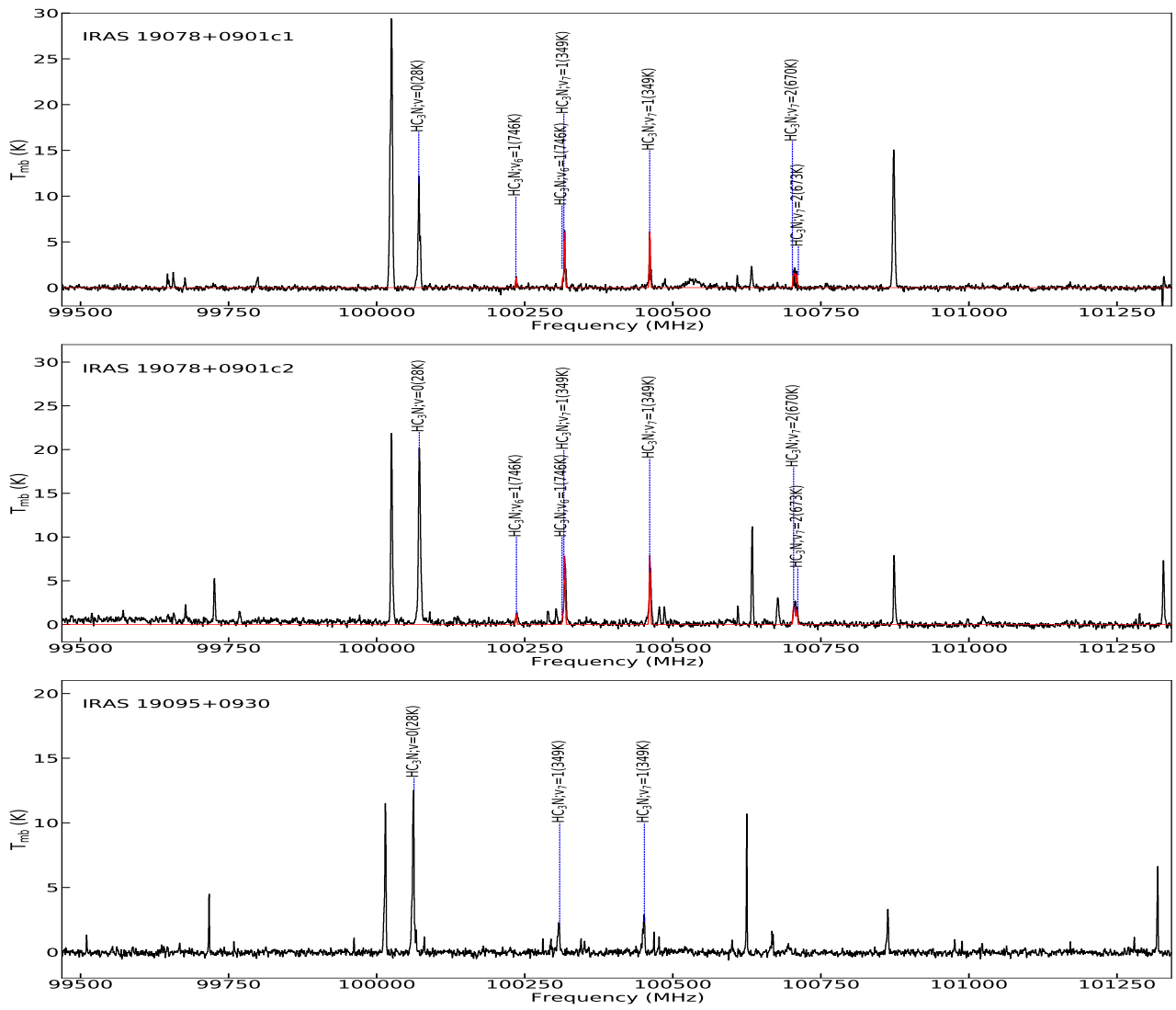


Fig. B.1: (continued.)

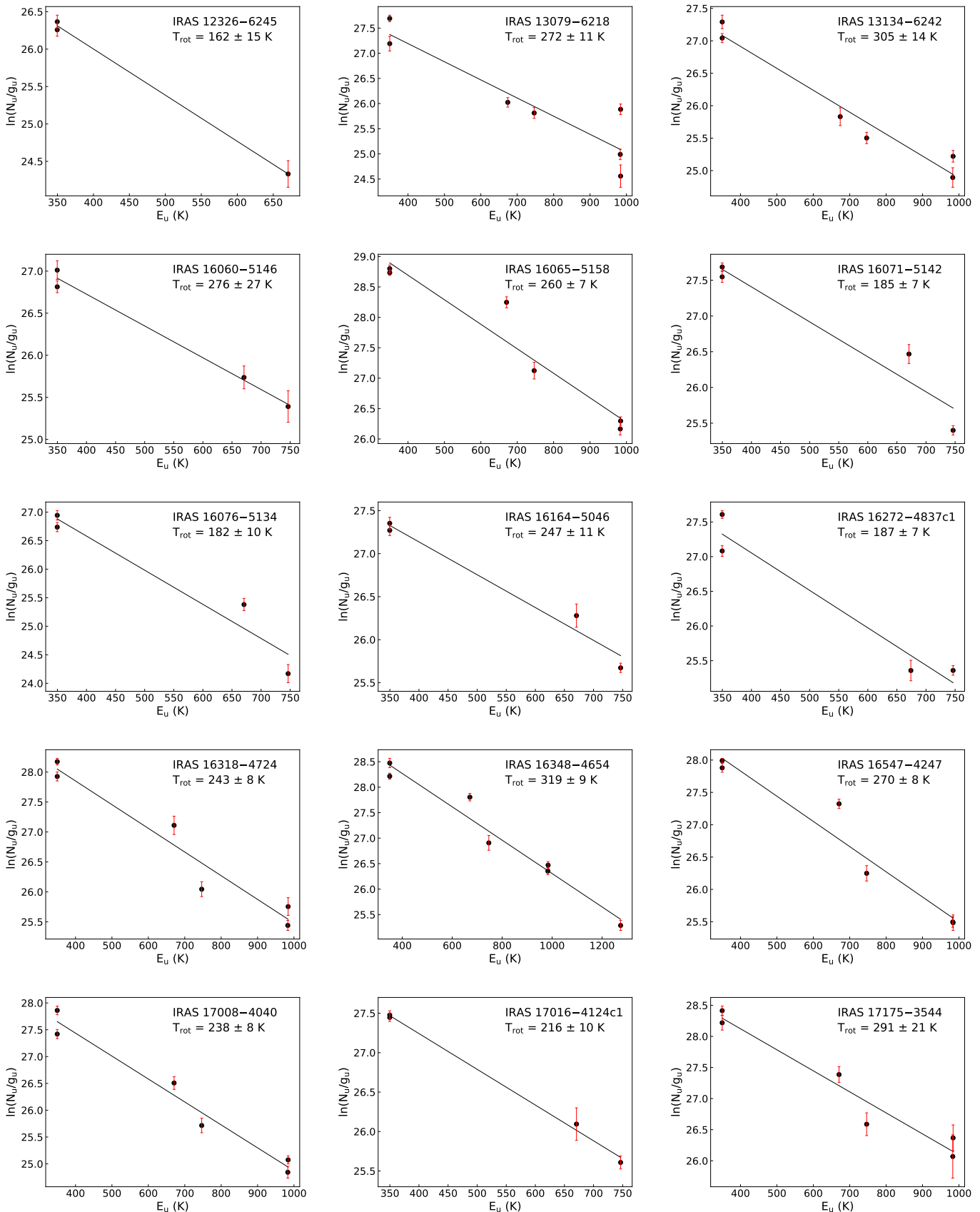


Fig. C.1: Rotational temperature diagrams for the observed HC_3N^* for 29 hot cores. The filled circles are for the observed transitions and the red lines indicate the error bar. The best least-squares fit is shown as the solid line.

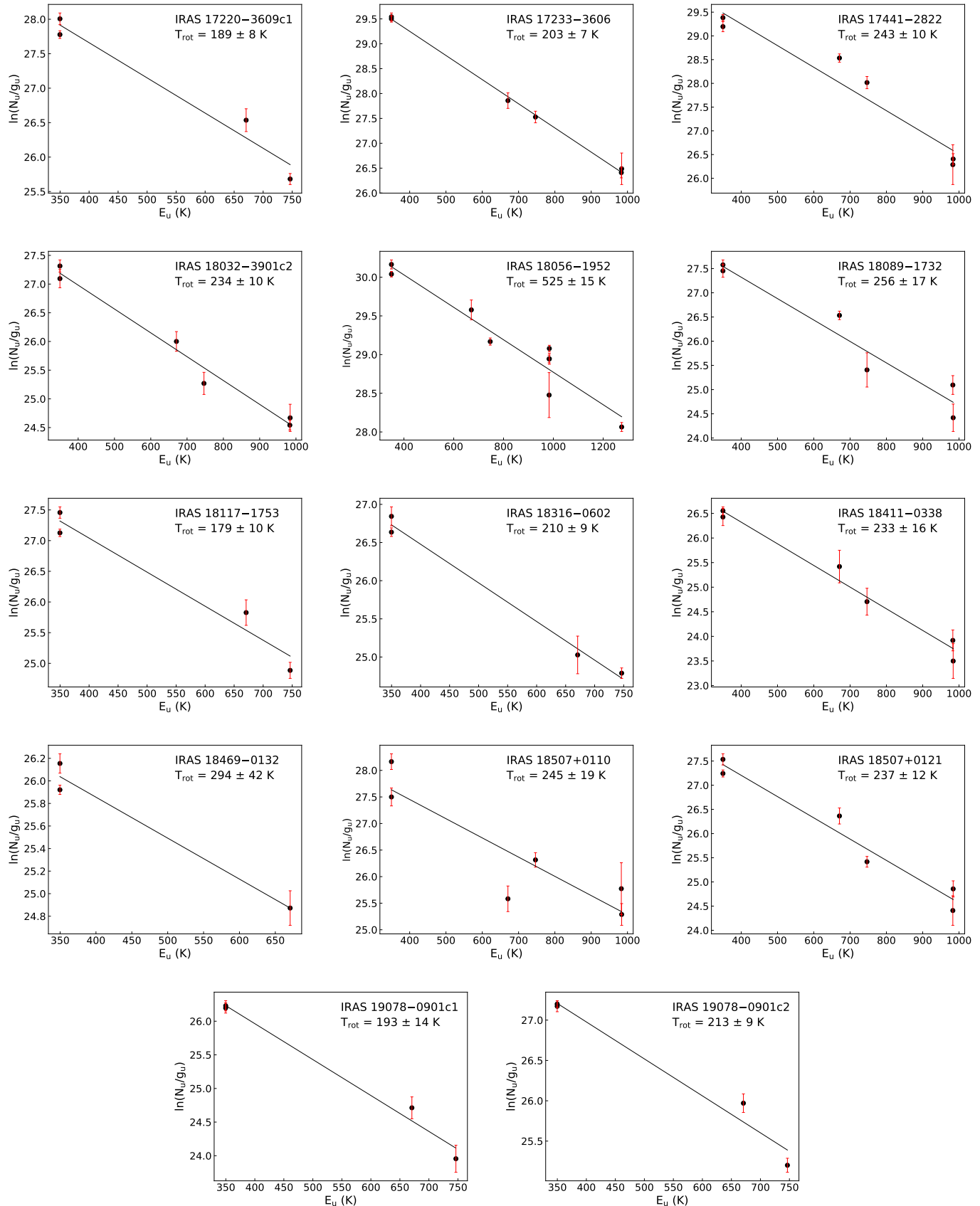


Fig. C.1: (continued.)